UPPSALA
UNIVERSITET

Digital Comprehensive Summaries of Uppsala Dissertations from the Faculty of Science and Technology 1592

Ultrafast Structural and Electron Dynamics in Soft Matter Exposed to Intense X-ray Pulses

OLOF JÖNSSON

ACTA
UNIVERSITATIS
UPSALIENSIS
UPPSALA
2017

ISSN 1651-6214
ISBN 978-91-513-0134-1
urn:nbn:se:uu:diva-331936

Dissertation presented at Uppsala University to be publicly examined in Polhemssalen, Lägerhyddsvägen 1, Uppsala, Friday, 15 December 2017 at 09:15 for the degree of Doctor of Philosophy. The examination will be conducted in English. Faculty examiner: Professor Jörgen Larsson (Lunds universitet).

Abstract

Jönsson, O. 2017. Ultrafast Structural and Electron Dynamics in Soft Matter Exposed to Intense X-ray Pulses. *Digital Comprehensive Summaries of Uppsala Dissertations from the Faculty of Science and Technology* 1592. 78 pp. Uppsala: Acta Universitatis Upsaliensis. ISBN 978-91-513-0134-1.

Investigations of soft matter using ultrashort high intensity pulses have been made possible through the advent of X-ray free-electrons lasers. The last decade has seen the development of a new type of protein crystallography where femtosecond dynamics can be studied, and single particle imaging with atomic resolution is on the horizon. The pulses are so intense that any sample quickly turns into a plasma. This thesis studies the ultrafast transition from soft matter to warm dense matter, and the implications for structural determination of proteins.

We use non-thermal plasma simulations to predict ultrafast structural and electron dynamics. Changes in atomic form factors due to the electronic state, and displacement as a function of temperature, are used to predict Bragg signal intensity in protein nanocrystals. The damage processes started by the pulse will gate the diffracted signal within the pulse duration, suggesting that long pulses are useful to study protein structure. This illustrates *diffraction-before-destruction* in crystallography.

The effect from a varying temporal photon distribution within a pulse is also investigated. A well-defined initial front determines the quality of the diffracted signal. At lower intensities, the temporal shape of the X-ray pulse will affect the overall signal strength; at high intensities the signal level will be strongly dependent on the resolution.

Water is routinely used to deliver biological samples into the X-ray beam. Structural dynamics in water exposed to intense X-rays were investigated with simulations and experiments. Using pulses of different duration, we found that non-thermal heating will affect the water structure on a time scale longer than 25 fs but shorter than 75 fs. Modeling suggests that a loss of long-range coordination of the solvation shells accounts for the observed decrease in scattering signal.

The feasibility of using X-ray emission from plasma as an indicator for hits in serial diffraction experiments is studied. Specific line emission from sulfur at high X-ray energies is suitable for distinguishing spectral features from proteins, compared to emission from delivery liquids. We find that plasma emission continues long after the femtosecond pulse has ended, suggesting that *spectrum-during-destruction* could reveal information complementary to diffraction.

Keywords: X-ray free-electron laser; Serial Femtosecond Crystallography; Radiation Damage; Plasma Simulations; Ultrafast Lasers; X-ray Imaging; Diffraction Theory; Ultrafast Phenomena; Hit Detection; Plasma Emission Spectra; Serial Femtosecond Crystallography; Protein Structure; Protein Crystallography; Metalloprotein; Non-thermal Heating; Water; Ferredoxin; NLTE Simulation; XFEL; FEL; SFX

Olof Jönsson, Department of Physics and Astronomy, Molecular and Condensed Matter Physics, Box 516, Uppsala University, SE-751 20 Uppsala, Sweden. Department of Cell and Molecular Biology, Molecular biophysics, Box 596, Uppsala University, SE-75124 Uppsala, Sweden.

ISSN 1651-6214
ISBN 978-91-513-0134-1
urn:nbn:se:uu:diva-331936 (http://urn.kb.se/resolve?urn=urn:nbn:se:uu:diva-331936)

Dedicated to all the samples that are destroyed in experiments every day.
Your destruction shall not be in vain!

List of papers

This thesis is based on the following papers which are referred to in the text by their Roman numerals.

I C. Caleman, N. Tîmneanu, A. V. Martin, H. O. Jönsson, A. Aquila, A. Barty, H. A. Scott, T. A. White, and H. N. Chapman, "Ultrafast self-gating Bragg diffraction of exploding nanocrystals in an X-ray laser," *Optics Express*, 23:1213, 2015.

II H. O. Jönsson, N. Tîmneanu, C. Östlin, H. A. Scott, and C. Caleman, "Simulations of radiation damage as a function of the temporal pulse profile in femtosecond X-ray protein crystallography," *Journal of Synchrotron Radiation*, 22:256, 2015.

III H. O. Jönsson*, C. Östlin*, H. A. Scott, H. N. Chapman, S. Aplin, N. Tîmneanu, and C. Caleman, "FreeDam – A Webtool for Free-Electron Laser-Induced Damage in Femtosecond X-ray Crystallography," *Manuscript, submitted*.

IV K. Nass, L. Foucar, T. R. M. Barends, E. Hartmann, S. Botha, R. L. Shoeman, R. B. Doak, R. Alonso-Mori, A. Aquila, S. Bajt, A. Barty, R. Bean, K. R. Beyerlein, M. Bublitz, N. Drachmann, J. Gregersen, H. O. Jönsson, W. Kabsch, S. Kassemeyer, J. E. Koglin, M. Krumrey, D. Mattle, M. Messerschmidt, P. Nissen, L. Reinhard, O. Sitsel, D. Sokaras, G. J. Williams, S. Hau-Riege, N. Tîmneanu, C. Caleman, H. N. Chapman, S. Boutet, and I. Schlichting, "Indications of radiation damage in ferredoxin microcrystals using high-intensity X-FEL beams," *Journal of Synchrotron Radiation*, 22:225, 2015.

V K. R. Beyerlein*, H. O. Jönsson*, R. Alonso-Mori, A. Aquila, S. Bajt, A. Barty, R. Bean, J. E. Koglin, M. Messerschmidt, D. Ragazzon, D. Sokaras, G. J. Williams, S. Hau-Riege, S. Boutet, H. N. Chapman, N. Tîmneanu, C. Caleman, "Ultrafast non-thermal heating of water initiated by an X-ray laser," *Manuscript, in review*.

VI H. O. Jönsson, C. Caleman, J. Andreasson, N. Tîmneanu , "Hit detection in Serial Femtosecond Crystallography using X-ray spectroscopy of plasma emission," *IUCrJ*, 4:6, 2017.

*These authors contributed equally to the work.
Reprints were made with permission from the publishers.

List of additional papers

Papers related to the subject, but not included in the thesis.

VII M. M. Seibert, T. Ekeberg, F. R. N. C. Maia, M. Svenda, J. Andreasson, O. Jönsson, D. Odić, B. Iwan, A. Rocker, D. Westphal, M. Hantke, D. P. DePonte, A. Barty, J. Schulz, L. Gumprecht, N. Coppola, A. Aquila, M. Liang, T. A. White, A. Martin, C. Caleman, S. Stern, C. Abergel, V. Seltzer, J.-M. Claverie, C. Bostedt, J. D. Bozek, S. Boutet, A. A. Miahnahri, M. Messerschmidt, J. Krzywinski, G. Williams, K. O. Hodgson, M. J. Bogan, C. Y. Hampton, R. G. Sierra, D. Starodub, I. Andersson, S. Bajt, M. Barthelmess, J. C. H. Spence, P. Fromme, U. Weierstall, R. Kirian, M. Hunter, R. B. Doak, S. Marchesini, S. P. Hau-Riege, M. Frank, R. L. Shoeman, L. Lomb, S. W. Epp, R. Hartmann, D. Rolles, A. Rudenko, C. Schmidt, L. Foucar, N. Kimmel, P. Holl, B. Rudek, B. Erk, A. Hömke, C. Reich, D. Pietschner, G. Weidenspointner, L. Strüder, G. Hauser, H. Gorke, J. Ullrich, I. Schlichting, S. Herrmann, G. Schaller, F. Schopper, H. Soltau, K.-U. Kühnel, R. Andritschke, C.-D. Schröter, F. Krasniqi, M. Bott, S. Schorb, D. Rupp, M. Adolph, T. Gorkhover, H. Hirsemann, G. Potdevin, H. Graafsma, B. Nilsson, H. N. Chapman, and J. Hajdu, "Single mimivirus particles intercepted and imaged with an X-ray laser," *Nature*, 470:78, 2011.

VIII T. Ekeberg, M. Svenda, C. Abergel, F. R. N. C. Maia, V. Seltzer, J.-M. Claverie, M. Hantke, O. Jönsson, C. Nettelblad, G. van der Schot, M. Liang, D. P. DePonte, A. Barty, M. M. Seibert, B. Iwan, I. Andersson, N. D. Loh, A. V. Martin, H. Chapman, C. Bostedt, J. D. Bozek, K. R. Ferguson, J. Krzywinski, S. W. Epp, D. Rolles, A. Rudenko, R. Hartmann, N. Kimmel, and J. Hajdu, "Three-dimensional reconstruction of the giant mimivirus particle with an X-ray free-electron laser," *Physical Review Letters*, 114:098102, 2015.

IX T. Ekeberg, M. Svenda, M. M. Seibert, C. Abergel, F. R. N. C. Maia, V. Seltzer, D. P. DePonte, A. Aquila, J. Andreasson, B. Iwan, O. Jönsson, D. Westphal, D. Odić, I. Andersson, A. Barty, M. Liang, A. V. Martin, L. Gumprecht, , H. Fleckenstein S. Bajt, M. Barthelmess, N. Coppola, J.-M. Claverie, N. D. Loh C. Bostedt, J. D. Bozek,

J. Krzywinski, M. Messerschmidt, M. J.Bogan, C. Y. Hampton, R. G. Sierra, M. Frank, R. L. Shoeman, L. Lomb, L. Foucar, S. W. Epp, D. Rolles, A. Rudenko, R. Hartmann, A. Hartmann, N. Kimmel, P. Holl, G. Weidenspointner, B. Rudek, B. Erk, S. Kassemeyer I. Schlichting, L. Strüder, J. Ullrich, C. Schmidt, F. Krasniqi, G. Hauser, C. Reich, H. Soltau, S. Schorb, H. Hirsemann, C. Wunderer, H. Graafsma, H. N. Chapman, and J. Hajdu, "Single-shot diffraction data from the Mimivirus particle using an X-ray free-electron laser," *Scientific Data*, 3:160060, 2016.

X S. Kassemeyer, J. Steinbrener, L. Lomb, E. Hartmann, A. Aquila, A. Barty, A. V. Martin, C. Y. Hampton, S. Bajt, M. Barthelmess, T. R. Barends, C. Bostedt, M. Bott, J. D. Bozek, N. Coppola, M. Cryle, D. P. DePonte, R. B. Doak, S. W. Epp, B. Erk, H. Fleckenstein, L. Foucar, H. Graafsma, L. Gumprecht, A. Hartmann, R. Hartmann, G. Hauser, H. Hirsemann, A. Hömke, P. Holl, O. Jönsson, N. Kimmel, F. Krasniqi, M. Liang, F. R. Maia, S. Marchesini, K. Nass, C. Reich, D. Rolles, B. Rudek, A. Rudenko, C. Schmidt, J. Schulz, R. L. Shoeman, R. G. Sierra, H. Soltau, J. C. H. Spence, D. Starodub, F. Stellato, S. Stern, G. Stier, M. Svenda, G. Weidenspointner, U. Weierstall, T. A. White, C. Wunderer, M. Frank, H. N. Chapman, J. Ullrich, L. Strüder, M. J. Bogan, and I. Schlichting, "Femtosecond free-electron laser x-ray diffraction data sets for algorithm development," *Optics Express*, 20:4149, 2012.

XI K. R. Beyerlein, D. Dierksmeyer, V. Mariani, M. Kuhn, I. Sarrou, A. Ottaviano, S. Awel, J. Knoska, S. Fuglerud, O. Jönsson, S. Stern, M. Wiedorn, O. Yefanov, L. Adriano, R. Bean, A. Burkhardt, P. Fischer, M. Heymann, D. A. Horke, K. E. J. Jungnickel, E. Kovaleva, O. Lorbeer, M. Metz, J. Meyer, A. Morgan, K. Pande, S. Panneerselvam, C. Seuring, A. Tolstikova, S. Aplin, M. Roessle, T. A. White, H. N. Chapman, A. Meents and D. Oberthuer, "Mix-and-Diffuse Serial Synchrotron Crystallography," *IUCrJ*, 4:6, 2017.

XII H. N. Chapman, P. Fromme, A. Barty, T. A. White, R. A. Kirian, A. Aquila, M. S. Hunter, J. Schulz, D. P. DePonte, U. Weierstall, R. B. Doak, F. R. N. C. Maia, A. V. Martin, I. Schlichting, L. Lomb, N. Coppola, R. L. Shoeman, S. W. Epp, R. Hartmann, D. Rolles, A. Rudenko, L. Foucar, N. Kimmel, G. Weidenspointner, P. Holl, M. Liang, M. Barthelmess, C. Caleman, S. Boutet, M. J. Bogan, J. Krzywinski, C. Bostedt, S. Bajt, L. Gumprecht, B. Rudek, B. Erk, C. Schmidt, A. Hömke, C. Reich, D. Pietschner, L. Strüder, G. Hauser, H. Gorke, J. Ullrich, S. Herrmann, G. Schaller, F. Schopper, H. Soltau, K.-U. Kühnel, M. Messerschmidt, J. D. Bozek, S. P. Hau-Riege,

M. Frank, C. Y. Hampton, R. G. Sierra, D. Starodub, G. J. Williams, J. Hajdu, N. Tîmneanu, M. M. Seibert, J. Andreasson, A. Rocker, O. Jönsson, M. Svenda, S. Stern, K. Nass, R. Andritschke, C.-D. Schröter, F. Krasniqi, M. Bott, K. E. Schmidt, X. Wang, I. Grotjohann, J. M. Holton, T. R. M. Barends, R. Neutze, S. Marchesini, R. Fromme, S. Schorb, D. Rupp, M. Adolph, T. Gorkhover, I. Andersson, H. Hirsemann, G. Potdevin, H. Graafsma, B. Nilsson, and J. C. H. Spence, "Femtosecond X-ray protein nanocrystallography," *Nature*, 470:73, 2011.

XIII C. Östlin, N. Tîmneanu, H.O. Jönsson, T. Ekeberg, A. V. Martin, and C. Caleman, "Explosion mapping to aid spatial orientation in single particle imaging with X-ray lasers," *Manuscript, in review*.

Contents

1. Introduction

1.1 Determining macromolecular structures

Life as we know it would not be possible without proteins and polynucleotides. These macromolecules are the building blocks of all life, but their structure and functions were unknown for a long time. When Kendrew *et al.* determined the first protein structure in 1958 [1], they were surprised and perhaps even disappointed. They had expected a simple underlying principle true for all protein structures, perhaps one as beautiful and symmetric as the helical structure of the DNA molecule that was determined a few years earlier [2, 3, 4, 5]. The DNA molecule functions as an information carrier in biology, and the beautiful linear repeating double helix seems to fit the role perfectly, like a long line of text. The protein structure solved by Kendrew *et al.* was on the other hand very complex and without symmetry. The myoglobin structure they solved was just one among a myriad of possible protein structures, not a universal template that could be applied to every other known protein. This quickly turned out to be the explanation why proteins can carry out so many different functions: catalysis, signaling, structural support, storage, transport and more. All proteins have a unique fold that is very difficult to estimate based on simple measurements. The feature that made protein structures interesting to study turned out to be the reason why the studies would be difficult.

A protein is a folded string built up from small molecules, amino acids, called residues when they form a polymer. The backbone of a protein is always the same repeating pattern of amino bonds between the amino acid residues. Each amino acid has a different side chain, that determines the chemical properties, such as hydrophobicity, size, pKa and bonding properties. There are 20 biogenic varieties of amino acids (and a few more in special cases), and the order in which they are assembled determines the folding and function of the protein. The structure of a protein can be separated into different conceptual layers. The primary structure is the order of the amino acids. This can either be determined by biochemical methods [6] or by prediction from the corresponding genetic code from mRNA or DNA. This rarely gives more than an estimate of how a protein will function, but can give clues about its general group. The secondary and tertiary structures are defined by how the backbone is folded and bound with itself with hydrogen bonds or disulfide bridges, and how the side chains interact with each other and the surroundings. The full structure is defined not only by its amino acids, but also by cofactors such as bound metal ions, prosthetic groups and structural water [7]. Figure 1.1

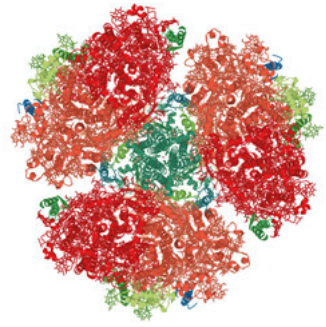

Figure 1.1. Model of a protein structure, the important membrane protein complex photosystem I from *Thermosynechococcus elongatus*, structure 3PCQ in the protein data bank [Paper XII]. This complex was the first to be investigated using serial femtosecond crystallography at the LCLS X-ray sulfur laser. Models such as this one can be used to explain the function of the protein.

shows a model of a membrane protein complex, photosystem I, that consists of several subunits and small molecules.

The method that has been most successful in determining protein structures is X-ray crystallography. A vast majority of the over 100000 protein structures solved to date has been determined with this method using synchrotron radiation. In X-ray crystallography, the sample is prepared as a crystal consisting of many repeating subunits. When exposed to X-rays, the elastic scattering from the crystals will form a diffraction pattern consisting of Bragg spots. After data processing the result is an observed electron density. The actual structure will be an interpretation of this, where the primary structure and known cofactors are fitted into the electron density map. Figure 1.2 illustrates the many steps from sample to model.

Even though protein crystallography is a very successful method in structural biology, there are some areas open for improvement. The crucial step of finding the experimental scheme of how to create a crystal is in many cases a process that requires much effort and time. Even when crystallization conditions are found, the process might be very sensitive and in many cases only produce very small crystals that will not diffract efficiently using synchrotron radiation, or that will be damaged by the beam [Paper XII] before enough data is collected. A whole class of important proteins is almost entirely absent from the databases. Membrane proteins make up almost half of all drug targets [8] and around 30% of all proteins in a typical organism [9]. The ratio of known membrane protein structures to all known structures was until recently very low (around 1–2% [10]). One of the main explanations is that membrane proteins are very difficult to crystallize into large crystals.

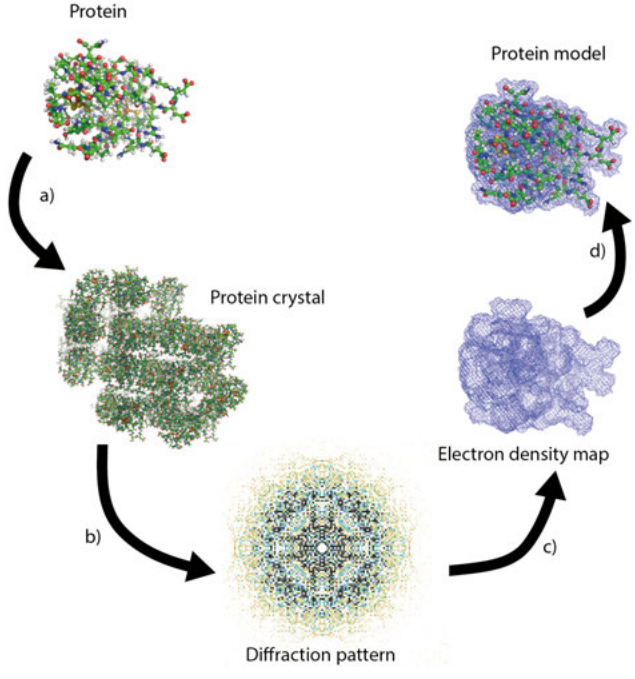

Figure 1.2. Schematic illustration of how protein crystallography can be used to get a model of protein structure. The protein needs to be a) crystallized into a protein crystal, b) put into an X-ray beam, where the crystal will diffract the incoming X-rays to form a diffraction pattern. Here only one pattern is shown, but ideally patterns from all angles should be collected. c) The diffraction patterns are then reconstructed into an electron density map. d) When the observed electron density is known, the protein can be fitted into it. One of the main aims of this thesis is to see how the light-matter interaction of intense radiation will affect a diffraction pattern from a protein crystal.

1.2 Studies of radiation damage

It only took four years after the first protein structure was determined until systematic studies were conducted to investigate if the result was influenced by the method. In 1962 Blake and Phillips used a sealed copper tube hard X-ray source to investigate how myoglobin protein crystals were affected by radiation. It was found that a single photon deposited enough energy to disrupt up to 160 individual protein molecules in the crystal. They created a model for radiation damage, that described the sample after exposure as consisting of three parts. The first part was the amorphous part that was destroyed and did not contribute to the scattered signal, resulting in a weaker total signal. The second part was the unchanged sample that fully contributed to the diffracted signal. The third part of the sample was modeled as a disordered part that scattered less at high angles. The consequence if some fraction of the protein belongs to the third part will be that information about certain length scales in the material are more affected by radiation damage. If the signal corresponding to the fine details of the material disappears, the resolution will be limited and high resolution structure determination will be impossible. When the dose, or number of photons reaching the sample, is increased, the damaged fractions would also increase. For a long time this was the leading picture of radiation damage: a dose dependent decrease of resolution and total signal [11]. It should be mentioned that local radiation damage was also seen in the first studies in addition to the global effects described above. Local or specific radiation damage is a term that is used today to describe specific changes from the native structure that are not uniform throughout a certain length scale. The metric often used for absorbed dose is energy absorbed per unit of mass, measured in gray (1 Gy is 1 J kg^{-1}). Many experiments aimed to find what dose was acceptable for different kind of energies and samples. Later models of radiation damage often add another factor in addition to the dose: the dose rate, measured in gray/second (Gy s^{-1}). It was found that the quality of the data was not only affected by the total dose, but also how the dose is delivered over time. It is not easy to predict the exact effects of an increased dose rate, but there are models available [12]. The absorption coefficient dependent upon element composition and size of the crystal can be calculated either by empirical formulas or using more detailed codes such as RADDOSE [13]. If the beam parameters are known, the maximum time in a beam with a certain energy and intensity can be calculated [14].

Among the many schemes to reduce the effects of radiation damage, cryocooling is the most widely used. Much of the damage at room temperature conditions can be attributed to radicals that will diffuse in the sample and break bonds. If the sample is cooled to very low temperatures, the radicals will be trapped and an increased dose is possible. A dose limit of 10 MGy per desired Å of resolution as suggested by Holton *et al.* [14] is a commonly used radiation limit in crystallography today.

When using very short pulses, many of the long time-scale processes responsible for signal degradation become irrelevant. The dose tolerance is claimed to be some orders of magnitude higher in the serial femtosecond crystallography (SFX) case (30 GGy) than in synchrotron crystallography [15]. The principle of diffraction-before-destruction was first proposed in 2000 [16]. When the intensity is so high that the sample is probed by the X-ray pulse before the onset of damage, the state of the sample after this interaction will not be a factor. The sample will in fact always explode during these high-intensity conditions. The benefit of using a very high intensity is that a smaller sample volume can be used. If a diffraction pattern from a small crystal, or even an image from a single molecule, can be collected fast enough, then the ultimate fate of the sample does not matter. Single particle imaging (SPI) of biomolecules was one of the main scientific cases that led to the construction of X-ray free-electron lasers that could produce short and intense X-ray pulses.

1.3 Science with X-ray free-electron lasers

As described above, there is room for new protein structure determination methods. One of the promising techniques is to use extremely intense X-ray photons generated in a free-electron laser (FEL). Here extremely intense pulses with an ultrashort duration can be produced. This allows the use of nanocrystals which would give a too weak signal under the conditions at a conventional synchrotron X-ray source.

The FEL was demonstrated in 1977 [17] after being proposed a few years earlier by Madey [18]. It operated in the infrared regime at a wavelength of 3.5 micrometers. Since then, several facilities have begun operations. In 2005 the first soft X-ray free-electron laser, FLASH, came into operation [19]. Many experiments have since been performed there, among others investigations of plasmas [20] and single shot diffractive imaging [21, 22]. In 2009 the first hard X-ray source was commissioned, LCLS in the US [23]. At the moment of writing, several more X-ray free-electron lasers are in operation or are under construction, such as FERMI in Italy [24], SACLA in Japan [25], European XFEL [26] in Germany and Swiss FEL in Switzerland [27].

The energy of the photon pulse in an X-ray free-electron laser comes from the conversion of kinetic energy from accelerated electrons into photons. When an electron travels in a magnetic field it will change its path and emit radiation. In the FEL, a high number of electrons are first generated from a pulsed source, and then accelerated to relativistic velocities in a linear accelerator. They then pass through a periodic structure of magnets called an undulator. When the high velocity electrons are forced to change direction by the magnetic field, they will emit light in the forward direction. Initially the electrons will radiate incoherently. Due to the so called “ponderomotive” force the electromagnetic radiation emitted will also affect the electrons. The electrons that

are in front of the phase of the radiation will lose kinetic energy to the radiation, and those behind will gain energy from the radiation. The resulting forces on the electrons will result in a microbunching effect where the electrons are packed together and periodically distributed along the undulator in the electron beam. When many electrons travel together they will act as larger charged particles, and will emit radiation coherently. The bunching properties of coherent radiation interaction with the electrons will cause the electrons to bunch up even more, creating an exponential gain along the undulator. This self-amplifying spontaneous emission (SASE) is the explanation for the extreme properties of a free-electron laser: its coherence, short pulse durations and high peak brilliance. Compared to a synchrotron, an X-ray FEL can produce nine orders of magnitude more intense light. New fields of science have been opened up when the combination of short and intense X-ray pulses is available [28].

Using ultrashort X-ray pulses, extreme states of matter can be created and studied with high time resolution. This enables studies of ultrafast phenomena in solids [29, 30]. Solid aluminum has been turned transparent due to heavy ionization, where further absorption has been saturated [20]. In FELs, different spectroscopy techniques have been used to measure temperatures of several eV reached within only a few fs [31]. Systems with double core-holes or even fully depleted of electrons have been studied [32]. Very small plasmas, nanoplasmas, have been created and studied [33].

One of the original motivations for developing FELs with beamlines for detecting scattered light was single particle imaging. The concept was experimentally proven to work at hard X-ray sources [Papers VII, VIII and IX]. So far however, no protein structure has been published using only a single protein. Instead, another type of experiment dominates in structural biology using FELs: the SFX experiment [Paper XII]. In the SFX method many small nanocrystals are exposed in series to X-ray pulses. The high intensity allows for crystals much smaller than what is needed to get a good signal using a synchrotron. High resolution structures have been solved, and new insights into biological questions have been made possible [34]. The possibility to use very small crystals has been used for new methods such as *in vivo* crystallization of protein crystals [35], and the ultrashort pulses have been used for time-resolved studies [36]. However, photon-matter interactions that cause heavy ionization and subsequent sample fragmentation are not fully understood and may influence structural determination despite the very short timescales [37].

In order to understand the scope of this thesis it can be useful to briefly describe a typical SFX experiment, as illustrated in Figure 1.3. The protein is prepared as a suspension of crystals with a size below 1 micrometer. It is non-trivial to deliver the sample into the vacuum chamber and make it align with the X-ray pulses. Often a gas dynamic virtual jet nozzle (GDVN) is used to focus the sample into a liquid jet with a radius around a few micrometers. Protein crystals with unknown orientation are then delivered into the interac-

tion region within a delivery liquid. When the sample is intercepted by an X-ray pulse, it will scatter at a CCD detector. High scattering angles represent information from short distances within the sample. The measured intensity on the detector will be a combination of diffraction from the crystal, called Bragg signal, and scattering from the delivery liquid. The crystals are hit at a random orientation, and the merging and indexing of diffraction patterns into a fully sampled reciprocal space map require extensive data analysis.

The following interesting aspects of soft matter in high intensity short pulse X-ray experiments are addressed in this thesis:

- The resolution-dependent Bragg signal as a function of ionization and atomic displacement in protein nanocrystals (Papers I and II)
- How temporal pulse profile variation will affect the diffracted signal (Paper II)
- How ionization, temperature and atomic displacement vary by sample and beam parameters (Papers III)
- Local damage in a metalloprotein (Paper IV)
- Heating and ionization of sample delivery liquids (Paper V)
- Photon emission from proteins and sample delivery liquids turning into plasma (Paper VI)

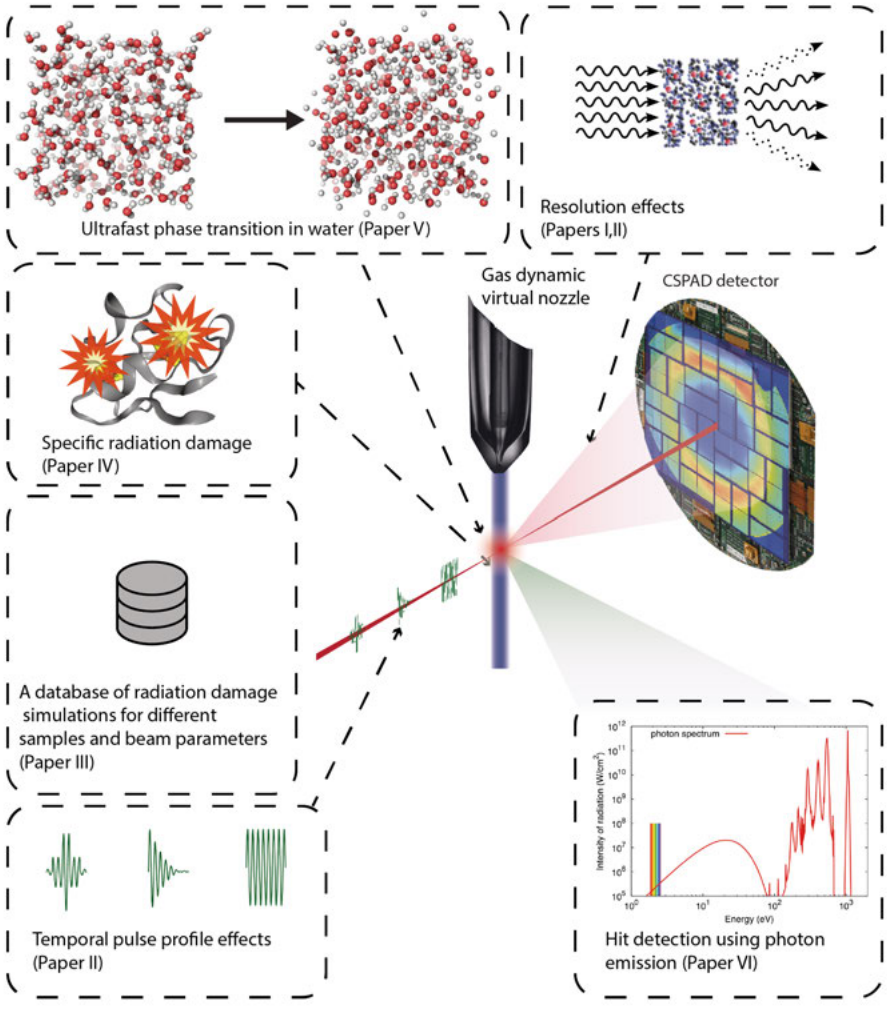

Figure 1.3. This thesis covers different aspects of an SFX experiment, as indicated by the dashed boxes. From top left clockwise: Electron and structural dynamics in a liquid jet sample delivery system investigated by experiments and modeling; dynamics of resolution dependent signal decay and self-termination by intense pulses; a feasibility investigation of hit detection using photon emission from protein crystals turning into plasma; effects of varying temporal pulse profile; a database of radiation damage in different samples and experiment configurations; an experimental study of local radiation damage in ferredoxin.

2. Physical processes in soft matter exposed to X-ray radiation

2.1 Interaction between soft matter and X-ray photons

Soft matter physics is a subfield of condensed matter physics, where the physical behavior is affected by energies on the order of thermal fluctuations. This includes macromolecules such as proteins, that under normal circumstances might shift between different conformations without breaking covalent bonds. Room temperature corresponds to an average energy of 0.025 eV, and a carbon-carbon bond requires around 1 eV to break. X-ray photons have a much higher energy, and their interaction with matter will require a description that is very different from the changes between native configurations that are important in room temperature conditions.

When a high energy photon hits a protein crystal, there are a number of interaction processes to consider. Coherent elastic scattering is the process that is exploited to get the measured diffraction pattern in a protein structure determination experiment. To achieve atomic resolution photon wavelengths on the order of Ångströms are needed, corresponding to X-ray photons with energies around 2–15 keV. The relative contribution from different interactions changes with the X-ray photon energy, as illustrated in Figure 2.1. The ratio between diffraction and photoionization is in the favor of ionization at the wavelengths used for imaging and crystallography. For each scattered photon, the number of ionization events is between 20–32 for the most frequently occurring elements in biological samples [38].

At the beginning of an intense FEL pulse, the sample can be considered electrically neutral. Due to the heavy X-ray bombardment, most of the atoms or molecules in the sample will lose electrons during the experiment, and thus ionization and heating processes are very important to understand. Within femtoseconds, the high intensity of an X-ray laser will turn the system into many charged ions and free electrons, a plasma. The temperature will reach values corresponding to several tens of electron volts, or several tens of thousands of Kelvins. Table 2.1 lists the many types of light-matter interaction. In the following sections the processes most relevant in this high ionization level and high temperature regime will be introduced. There are two main aspects of ionization that will be described in this thesis; ionization dynamics and scattering from ionized samples. In most cases the perspective of high intensity crystallography in short timescales will be the focus. In addition, photon emission from plasmas will be discussed.

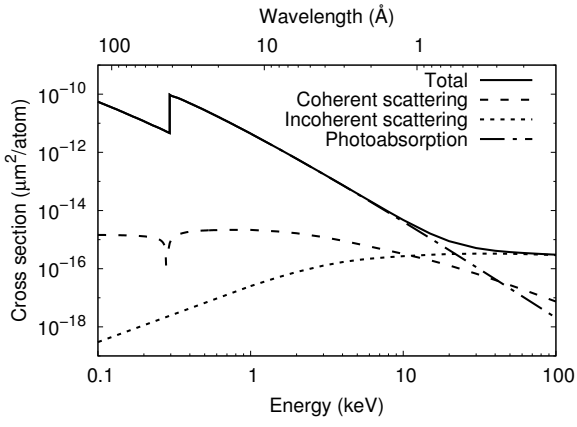

Figure 2.1. Contributions to photon cross section for carbon. In the photon energy range used in protein crystallography, photoionization is the dominating process.

2.1.1 Photon absorption

Light can be described both as a particle and as a wave. In the particle picture, the total energy is not only the number of photons but also the energy of the individual photons. In the wave picture, the wavelength and the intensity can be varied independently while maintaining the same total energy. These concepts were first understood around 100 years ago in a series of experiments and theoretical developments.

Table 2.1. *Important X-ray matter-interaction processes. List adapted from [39].*

Process	Inverse process
Photo ionization	Radiative recombination
Photo excitation	Spontaneous emission
Electron impact ionization	Three-body recombination
Electron impact excitation	Collision of the second kind
Autoionization	Dielectric recombination
Bremsstrahlung	Inverse Bremsstrahlung

When light hits a material it may eject electrons, provided that the photon energy is high enough. It was found that the number of ejected electrons has a linear relationship with the number of photons. More photons give more ejected electrons. If the energy of the photons is increased, the relationship will not be linear at all. When the energy is increased above certain thresholds, there is a large increment in the number of ejected electrons. This phenomenon, the so called photoelectric effect, was first explained theoretically by Einstein in his famous 1905 article [40]. He suggested that the cause was

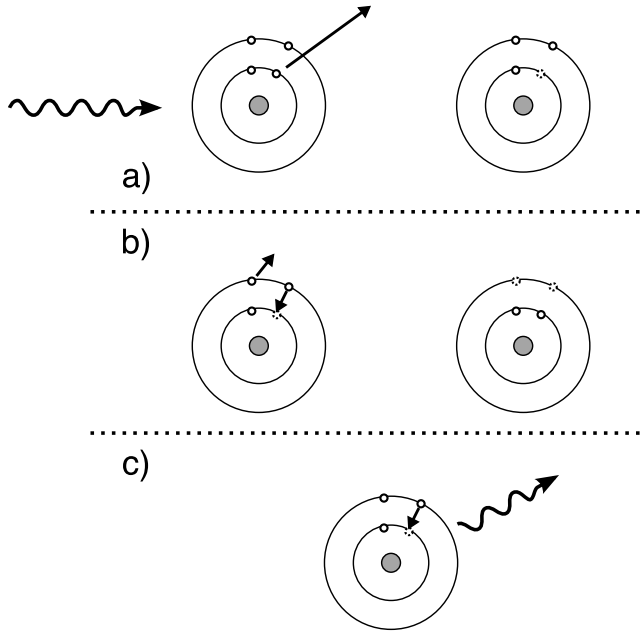

Figure 2.2. Schematic representation of ionization processes using a simple Bohr model with two populated core levels and two outer levels. a) In a photoionization process (left) the energy of a photon is used to remove a bound electron from the atom. A charged ion with a hole will be formed, in this case a core hole (right). b) Example of Auger process following photoionization. When an ion or atom is in an excited state it may relax into a lower energy state. The excess energy may leave the ion as electrons or photons. In this example, a valence electron falls down into the empty position at the core level, and the other valence electron gets the energy and leaves (left). An ion with two empty positions at the valence level is formed (right). c) Energy can also be conserved when the ion relaxes if a fluorescent photon is emitted.

that light was carried in discrete quantized packages with a fixed energy. In 1914, this was experimentally confirmed by Millikan [41].

The explanation for these thresholds is that electrons in matter are bound at distinct energy levels, meaning that the binding energy is quantized. If an incoming photon has higher energy than the binding energy, a photoionization process can occur, as illustrated in Figure 2.2. An electron will be ejected, with kinetic energy equal to the difference between the incoming energy and the binding energy. In electron spectrometry, the energy of the ejected electrons is measured and compared to that of the incoming light. The binding energies can then be deduced, which is an important property to understand in atoms, molecules and materials. Core electrons have a high binding energy, and are more tightly bound to the nucleus of atoms. Valence electrons have a lower

binding energy, and can be shared between atoms in a molecule, or be part of a band structure in a solid.

In the absorption process, the atoms and molecules will lose electrons and form ions. The cross section for photoionization increases with atomic charge number and decreases with an increase in photon energy (with the important exception of absorption edges) [39]. When very intense light is used, multiple ionizations can occur and high charge states can appear. High charge states have a lower cross section for further ionization [20].

For isolated atoms, the cross section for ionization of a bound electron has its maximum close to the binding energy. For the light elements present in proteins, this means that the ionization cross section for core electrons with ionization potentials around a few keV is relatively high.

2.1.2 X-ray scattering

In elastic scattering, a photon will interact with an ion, atom or molecule and change direction without losing energy. The scattering of photons on free electrons is called Thomson scattering. This is a very good approximation in typical X-ray crystallography.

Bragg's law describes how light will spread from a crystalline sample:

$$2d \sin \theta_{\mathrm{B}} = n\lambda \,, \tag{2.1}$$

where d is the distance between scattering planes, θ_{B} is the Bragg angle, n is a positive integer and λ is the wavelength of the incident light. It is often useful to use the magnitude of the momentum transfer $\vec{q}$, often described as $q = 2\pi/d$, instead of plane distances. In this picture, a certain scattering angle represents one length scale of spatial coherence in the electron density of the sample. Analysis of the scattered light gives information about the structure of the scattering matter.

In the ideal case, the signal from each unit cell in the protein crystals will interfere, and the intensity will gather in Bragg spots with an increase in intensity as the square of the number of unit cells. This amplification is the reason that synchrotron light can be used to determine the structures of proteins, even if the signal from a single protein is very weak. This amplification will work in the opposite direction when the crystal size goes down. Then the intensity of the light must be squared to keep up with the reduction in the number of unit cells and get the same scattered intensity. FELs provide the necessary intensity to get high enough signal intensity on the detector in the case of protein crystals in the sub-micrometer size range.

Incoherent scattering of an atom is an inelastic scattering process in which a photon will lose some energy, but not all, to the system. The wavelength of the outgoing photon will be longer, and the system will increase in energy, leaving the system in an excited but neutral state. If the scattering involves a molecule,

the process is called Raman scattering, if it involves a quasi-free charge it is called Compton scattering. This scattering will contribute to a diffuse background in crystallography and imaging. In general this will only decrease the signal to noise ratio. Normally the incoherent scattering from inelastic processes is problematic, as it will not be used for structural determination. From a photon spectroscopy point of view, these processes will broaden line emission on the way out of a sample.

2.2 Secondary ionization processes

2.2.1 Auger process

An ion in an excited state might relax into a state with lower energy. When this happens, the energy is released in a so called Auger process, as illustrated in Figure 2.2. The Auger process was discovered by Lise Meitner in 1922 [42], and by Pierre Auger in 1923 [43].

After a photoionization of a core electron, the formed ion will be left with a core-hole vacancy. If an electron falls from an outer shell into the empty place in the inner shell, the excess energy might be released either as fluorescence or as further ionization. The ratio of cross-section between fluorescence and electron ejection is in favor of fluorescence for deep core levels, present in heavier elements. The energy of this transition depends on the energy difference between the two states involved, and is characteristic for different elements. The transition is often called characteristic line emission. Very recently it was suggested that this fluorescence could be used for structural determination provided that very short pulses are used [44].

For lighter elements, such as the elements most common in proteins, electron ejection is more common. The released electron is called an Auger electron. The kinetic energy of the released electron will be the difference between the energy of the electronic transition and the ionization energy of the ejected electron. The lifetimes of core holes before an Auger electron is ejected can be measured as a broadening of the so-called Auger lines in the electron spectrum. These are on the order of femtoseconds for the light elements: 11.1 fs for C, 9.3 fs for N, 6.6 fs for O and 1.3 fs for S [45]. The chemical environment can also affect the lifetimes.

2.2.2 Electron impact ionization and electron cascades

If the electrons released in photo ionization and Auger processes do not leave the sample, they can interact with atoms and ions to cause further ionization. This secondary impact ionization mainly affects outer shell electrons. These electrons might in turn cause even more ionization, and create an electron cascade, as illustrated in Figure 2.3. Hundreds of secondary electrons might

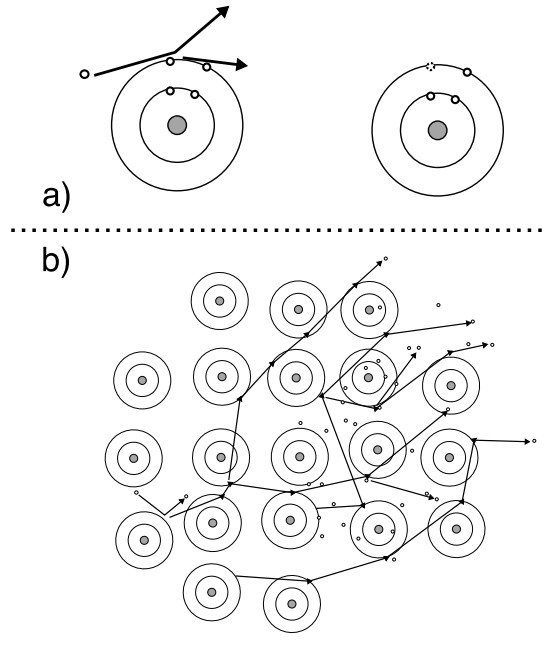

Figure 2.3. Schematic representation of ionization processes using a simple Bohr model with two populated core levels and two outer levels. a) Electron Impact Ionization is the process where an electron hits an atom, kicks out an additional electron and creates an ion. b) Both of these electrons can progress further in the material and create a cascade of more and more electrons. A single photoionization event can trigger hundreds of secondary ionization events, and due to the intense photon pulses at FELs, the average number of ionizations per atom can exceed one within a few femtoseconds [38].

be released from a single photoionization event depending on the energy of the incident photon [46]. The cross section for electron impact ionization changes with electron energy, element and ionization state. The maximum cross section is between a few eV and a hundred eV. Ionized atoms have a lower cross section [39].

The kinetic energy distribution of the generated electrons after a photoionization event is not equilibrated at first. The electron cascades develop on a timescale of femtoseconds to tens of femtoseconds, and will start to thermalize. The velocity distribution in the material consists of two parts, one with almost Maxwellian kinetic distribution (from secondary electrons and some Auger electrons) and one part that corresponds to higher velocities (photoelectrons). A fraction of the equilibrated electrons may even get higher energy than the incident photons [47].

2.3 Coulomb explosion and hydrodynamic expansion

During the X-ray exposure, the molecules in the crystal will rapidly be ionized creating a sample with positive ions and free electrons. If the electrons escape, the net charge will be positive and the atoms will repel each other. This process is called Coulomb explosion and dominates for small samples such as single proteins. If the sample volume is bigger and when most of the sample is ionized, the electrons cannot escape the positive center of the material. The kinetic energy is instead deposited by collisions, heating the samples and eventually leading to a Maxwellian distribution of kinetic energies. A hydrodynamic expansion will occur, where the inner core of the sample experiences a higher pressure due to the electrons colliding that will eventually spread to the outer layers of the sample. The outer layer of the sample will have a net positive charge and will peel off [48, 49].

FELs allow us to access very short timescales and mitigate the damage process in Coulomb explosions and hydrodynamics expansion. The timescale for these is typically picoseconds to nanoseconds. If the pulse is short enough, the photoelectron might not interact with the sample before the pulse is over. Using a small crystal in SFX gives the opportunity for the energetic electron to leave the sample due to low electron impact cross section at high electron energies. Auger electrons have a more local effect and will likely deposit all their energy in the sample [38].

2.4 Plasma

When a sample is exposed to high intense X-rays it will quickly be ionized and go through a rapid phase transition into a plasma. Generally a plasma can be described as fulfilling the following three criteria:

$$\lambda_{\mathrm{D}} << L \tag{2.2}$$

$$N_{\mathrm{D}} >>> 1 \tag{2.3}$$

$$\omega\tau > 1 \tag{2.4}$$

where the shielding distance or Debye length λ_{D} is much smaller than the size of the system L, the number of particles in the Debye sphere N_{D} is much larger than 1, and the frequency of the plasma oscillations ω times the collision rate between neutral atoms τ is larger than 1. In words, this means that the charged particles in the plasma will shield electric potentials and fields on a long range, and be influenced by each other on a short range, and that the motion of particles is described by electromagnetic forces rather than hydrodynamic forces. The free electrons can be seen as an electron gas. Compared

to the interactions in the more familiar phases gases, liquids or solids, different processes must be considered. The interactions between the free electrons and the ions are needed to describe this state. Processes such as electron impact ionization (as described in section 2.2.2) and recombinations where electrons recombine with ions to reduce the charge are common. Ionization potentials will experience a phenomenon called continuum lowering due to the strong fields, and the highest electronic levels will be easier to ionize, and in fact be part of a continuum rather than bound states.

The special case of plasma exposed to high intensity X-rays requires even more consideration. During the exposure more energy will be pumped into the system, and the continuous bombardment of photons will make the system highly dynamic. The high kinetic energy of the electrons may not be in equilibrium with the ion population, and the temperatures might differ by orders of magnitude. Typically the thermalization time of the electron kinetic energy distribution is in the femtosecond regime, and the ion-electron thermalization time is on the order of hundreds of femtoseconds. When the distributions are equilibrated, the kinetic energy will follow a thermal Maxwell-Boltzmann distribution. During the pulse, the system might get further away from an equilibrium situation when more energy is added. Bremsstrahlung effects, when charged particles change direction within the plasma, will create photons which in turn might ionize or excite further, changing the opacity and absorption cross sections.

Warm dense matter (WDM) is a loosely defined term that describes matter in high intensity X-rays. In the WDM regime, matter is too hot to use a condensed matter physics framework such as solid state physics, but not so hot to require the term "hot plasma", as seen in Figure 2.4. The degeneracy parameter $\Theta = \frac{T_e}{E_F}$ is the relation between the electron temperature T_e and the Fermi energy E_F and relates to how degenerate the system is. When the system is very degenerate ($\Theta << 1$) the system must be modeled using quantum treatment; for non-degenerate systems ($\Theta > 1$) statistical methods can be used. Due to the high temperatures involved, this parameter will rise above 1 in a few femtoseconds. The coupling parameter $\Gamma = \frac{\langle E_{\text{potential}} \rangle}{\langle E_{\text{kinetic}} \rangle}$ is the relation between the potential energy and the kinetic energy in the system, and is traditionally used to describe the physical regime of the system. When $\Gamma << 1$, the system is in the weakly coupled regime associated with room temperature conditions. In a high intensity situation, the system will be out of equilibrium and the coupling parameter will be closer to 1.

Early work in X-ray emission spectroscopy could reveal several important concepts in atomic physics such as the origin of the atomic number [50] and an experimental measurement of electron shells. When we approach high intensities and want to model high intensity X-ray interaction with a plasma, many processes must be considered. As the sample heats, a background of thermal radiation with increasing energy will form. Black body radiation is a

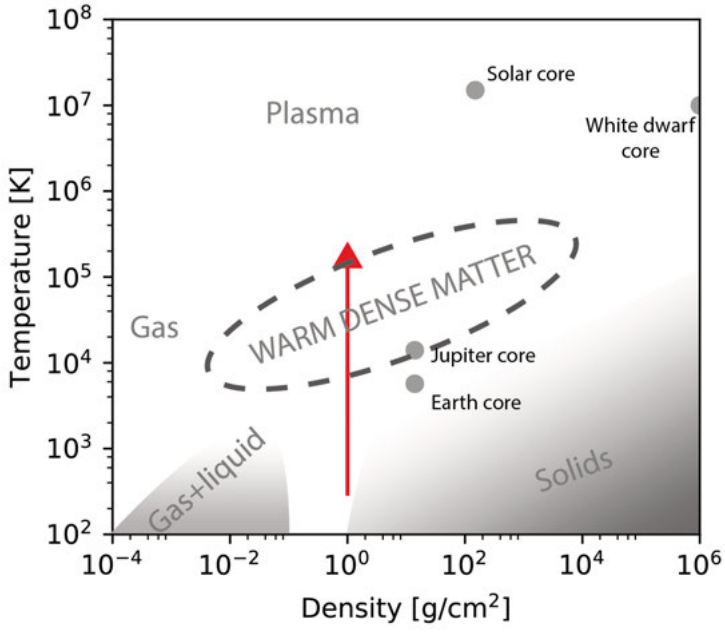

Figure 2.4. Temperature and densities of various systems. Shown with a red arrow is the rapid increase in temperature for a solid or soft matter sample in the interaction region of an FEL pulse. Temperatures of up to tens of eV, or hundred of thousands of K can be reached within a hundred femtoseconds.

continuous spectrum that depends on the temperature of the emitter. When the temperature increases, the distribution shifts to higher energies. In a heated plasma, this can stretch well into the extreme UV region or even into the soft X-ray region. Planck's law, which describes how the spectral radiance at a certain frequency ν depends on the temperature T, can be written as

$$B_\nu(\nu, T) = \frac{2h\nu^3}{c^2} \frac{1}{e^{\frac{h\nu}{k_B T}} - 1}, \tag{2.5}$$

where k_B is the Boltzmann constant, h is Planck's constant and c is the speed of light in the medium. The frequency of light is directly proportional to its energy E as $E = h\nu$.

Many electronic transfers in the sample will be accompanied by emission of photons. The same is also true in reverse; state specific absorption will also shape the spectra. In a plasma, not only bound states but also free states exist. Electronic transfers between all combinations are possible: bound-bound, free-bound, bound-free and free-free. Free-free transitions have a broad distribution, and consist of bremsstrahlung or inverse bremsstrahlung. The thermal background is built up from these transitions. The bound-bound transitions will be similar to those from atomic or molecular systems modified by shift effects. When electrons transfer between free and bound states, the emission will be broad in energy distribution. Peaks are often broadened due to the many complex interactions present. In addition to the above radiation, scattering from the incoming X-ray laser will be present, both from elastic and inelastic processes. At or very near the incoming energy, the spectra will be dominated by these effects. See Figure 2.5 for a schematic spectrum with its constituents. In general, complex modeling is required to predict an emission spectrum accurately.

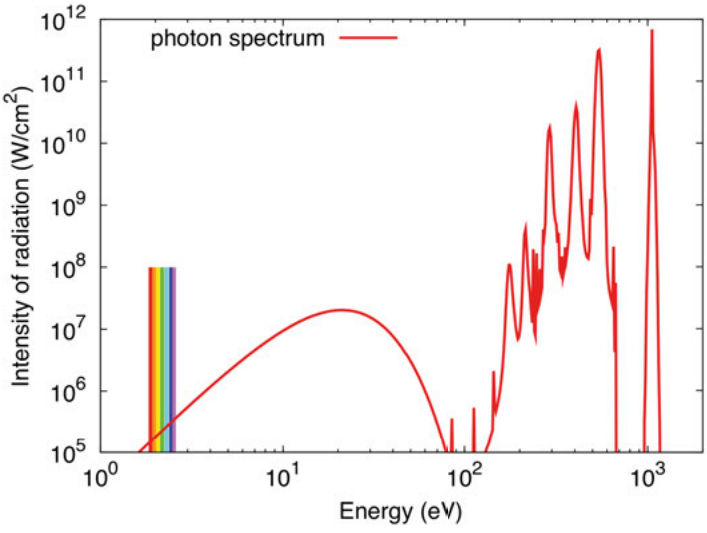

Figure 2.5. Schematic view of the many types of photon emission from a plasma. Features from low energy to high: Black body-like emission (with optical spectrum shown as a comparison), characteristic line emission in a continuous distribution of free-bound emission and scattering at the highest energy as a well formed peak.

3. Methods

This chapter will present the combination of modeling and experiments used in the thesis. The exact research questions vary, but the common factor among the research presented is a desire to understand the interaction of light and matter at high intensity and short pulses. Simulations and calculations are used to estimate radiation damage and calculate the intensity of the diffraction signal. An overview of the signal intensity calculations used in Papers I, II, III and V can be seen in Figure 3.1. The experiments that are part of this work were conducted at the CXI instrument at LCLS, currently the femtosecond protein crystallography beamline with the highest X-ray intensity.

3.1 Modeling

3.1.1 Non-thermal plasma code

The software code CRETIN is used in all the presented papers. The name is a contraction of "accretion", due to its origins in astrophysics as a tool to model accretion discs around black holes. CRETIN is a well-established [51] non-local thermodynamic equilibrium (NLTE) radiation transfer code that tracks the electronic population of the atoms and photon distributions in the system, and assumes that a plasma is formed [52, 53].

Simulations can be made in several dimensions and Figure 3.2 shows an example of a 1D simulation geometry. The simulation space is divided into quasi-neutral continuum zones with neutral net charge and mass conservation. Explicit particles or bonds are not described by the code. Electron and ion kinetic energies are modeled as being internally in a Maxwellian distribution within the zone. The electrons and ions are allowed to be out of thermal equilibrium in relation to each other and to neighboring zones, and heat and radiation are allowed to transfer between zones.

The code keeps track of the population of different electronic states and transitions between them. Processes important for systems exposed to intense radiation such as photoionization, electron collision excitation, Auger ionization and dielectric recombinations are included in the code. The code models a full radiation spectrum, including transport to neighbouring zones and absorption process. Continuum lowering using Stewart-Pyatt degeneracy lowering [54] is used to compensate for the lowering of ionization potentials. A hydrogenic atomic model is used. Non-bound electrons are assumed to be

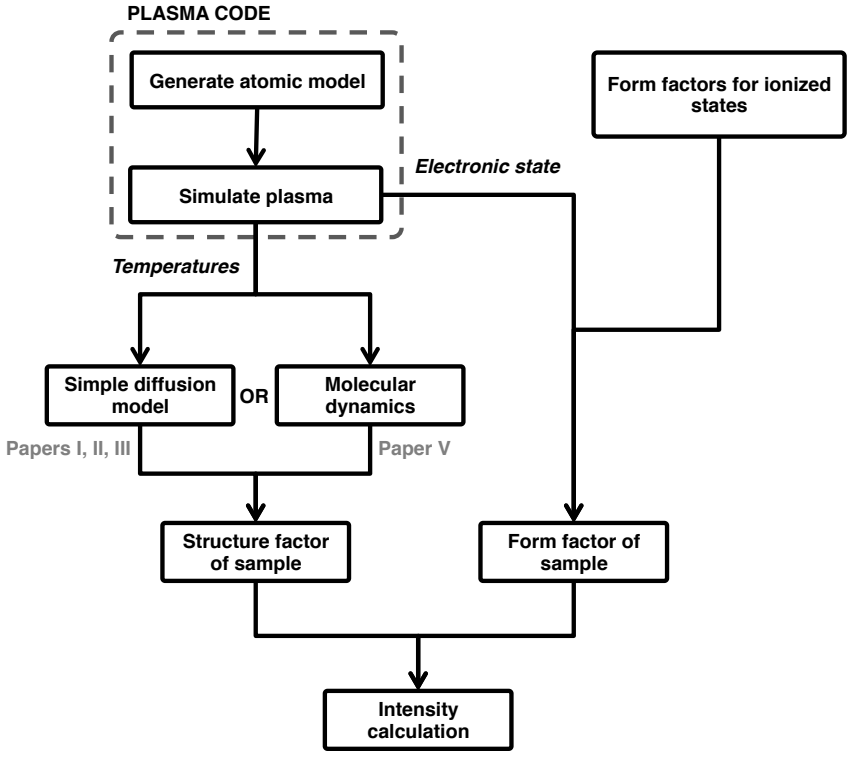

Figure 3.1. Flow chart of simulation methods. For Papers I, II and III a diffusion model using only temperatures and collision rates was used, and in Paper V, a more elaborate molecular dynamics model that treated particles explicitly was used. In the case of Papers I, II and V, the atomic form factors were calculated, and together with the structure factor, used to calculate the scattered signal. The end result is an estimate of how the damage processes affect the diffracted signal at a certain resolution.

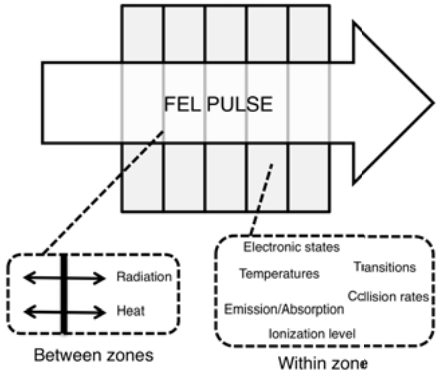

Figure 3.2. The sample is modeled as zones. Each zone is treated as a continuum where the element composition, temperatures, pressure and electron state population are the same. Explicit bonds and individual particles are not included in the calculation. Radiation and heat, but not mass, can transfer between zones, however the zones can be allowed to expand and contract. One of the main advantages of a continuum code is that large systems, such as a crystal in a water jet, can be simulated.

internally equilibrated in kinetic energy, and are represented by their density and a single temperature. The energy of the ions is treated separately, and their temperature is allowed to be different from the electron temperature. The ion temperature is used to calculate ion collisional excitations and ionizations. Radiation is tracked over a full photon spectrum. When the population of all electronic states and the radiation energies are known, the transition rates can be used to calculate the evolution of the system.

There are some limitations to the plasma continuum approach when simulating an SFX experiment: the lack of particle treatment given by a continuum model and the inherent plasma assumption. The fact that individual particles are not treated also gives the method its main strength, the ability to perform simulations of large systems in a computationally efficient way without sacrificing details in the atomic kinetics. There are alternative methods that may treat particle motion directly, relying on molecular dynamics [55, 32, 56, 57]. Our approach to handle this was used in Paper V where simulation parameters were matched with molecular dynamics simulations.

The fact that the code both requires a system in a plasma state and is able to predict why the system is in such a state may at first seem to be a case of circular logic. The main support for using the code even for this initial transition is that independent methods predict the highly ionized plasma state within the same timeframe. Initially the cross sections for neutral atoms are used to calculate the ionization rate in the code, and the high flux in all simu-

lated cases will be so high that the plasma assumption will be valid within 1–2 femtoseconds.

The model used here calculates average atomic displacements and ionization, and in turn provides a scaling of the Bragg intensities, but it does not treat the coherent dislocations (resulting in moving of the Bragg spots) or crystal explosion (resulting in changes in the widths of the Bragg spots). An experimental scenario is assumed where the crystals are delivered with a liquid jet into the interaction region; in this situation crystal expansion is limited by the surrounding water. This has been shown to be viable for the short time scale of the pulse [58]. Any coherence effects that could occur due to the rapid ionization of heavy atoms are also not taken into account. Such effects have been suggested by simulations to be useful for phasing [59].

3.1.2 Modeling elastic X-ray scattering from protein crystals

In the ideal case of a static protein crystal, the full Bragg signal from an undamaged sample at scattering vector $\vec{q}$ is calculated as

$$I_{\text{ideal}}(\vec{q}) = r_{\text{e}}^2 \Delta\Omega |F_0(\vec{q})|^2 I_0 \,, \tag{3.1}$$

where r_{e} is the classical electron radius, $\Delta\Omega$ is the solid angle of a pixel detector, $|F_0(\vec{q})|^2$ is the form factor particular for a sample [38] and I_0 is the beam intensity. In a diffraction experiment, the scattering vector $\vec{q}$ can be seen as the resolution, a spatial frequency in the sample, and measured in a diffraction experiment using a wavelength of λ at Bragg angle θ

$$q = 2\frac{\sin(\theta)}{\lambda} \,. \tag{3.2}$$

Higher scattering angles correspond to shorter sampling distances within the sample. This describes the situation in an ideal non-damaged sample.

In the non-ideal case, scattering will change during the pulse. First the effects of ionization are considered. When an atom is ionized once, it will decrease the scattering cross section by 12%–14% [38]. When half of the atoms in a crystal are ionized, the Bragg signals are reduced by 20% [15]. If the sample is exposed to extreme intensities, the decrease in cross section will be more important as the ionization levels increase [60]. This effect is not uniform across different scattering vectors. A decay factor $k(q,t)$ can be defined as a fraction: the signal of an ionized system in relation to the neutral system as a function of time t and scattering vector $\vec{q}$

$$k(q,t) = \frac{\langle f \rangle^2}{\langle f_0 \rangle^2} \,, \tag{3.3}$$

where the average of the atomic form factor $\langle f \rangle$ is a weighted sum

$$\langle f \rangle = \frac{\sum_i f_i(q,t) \cdot c_i}{\sum_i c_i}, \tag{3.4}$$

where $\sum_i$ is the sum over all ionized states including core holes for all elements present [61]. The fraction of ions c_i in state i is obtained from the plasma simulations for each time t. The factor $\langle f_0 \rangle$ represents the initial ideal state where all electron levels are filled, thus the factor $k(q,t)$ is 1 for the undisturbed crystal.

The form factor for an electronic state i can be parametrized according to the Cromer and Mann method [62] as a sum

$$f_i(sin(\theta)/\lambda) = \sum_{j=0}^{4} a_j e^{b_j (sin(\theta)/\lambda)^2} + c, \tag{3.5}$$

where the parameters a_j, b_j and c are defined as in Paper I, θ is the Bragg angle and λ is the wavelength. The scattering factors of an atom in different charge states can be seen in Figure 3.3.

Using the theory above, it is possible to describe the scattering as a function of the population of electronic states present, and their respective form factor dependencies of the scattering vector. As a general observation, the scattering at very low $\vec{q}$ will be depending on the overall ionization level. At higher scattering angles the ratio between filled and empty core levels becomes very important. If the core levels of the atoms are empty, the k factor at high scattering angles will be close to 0, and high resolution signals will be cut off.

In addition to changes in scattering due to electron loss from the atoms, the atom or ion positions can also be disturbed. To model how displacement in a crystal lattice affects the Bragg signal strength, we start with an estimate of the diffusion. In a plasma, the diffusion coefficient for an ion i is dynamic and can at time t be estimated as [63]

$$D_{\mathrm{i}}(t) = \frac{k_{\mathrm{B}} T_{\mathrm{i}}(t) \tau_{\mathrm{i}}(t)}{m_{\mathrm{i}}}, \tag{3.6}$$

where k_{B} is the Boltzmann constant and m_{i} is the ion mass. Ion temperature T_{i} and ion-ion collision rate $\tau_{\mathrm{i}}(t)$ will increase during the pulse as calculated from the plasma code.

The root mean square displacement as a function of time is given by

$$\sigma_{\mathrm{i}}(t) = \sqrt{2N \int_0^t D_{\mathrm{i}}(t')\mathrm{d}t'}, \tag{3.7}$$

where $\sigma_{\mathrm{i}}(t)$ depends on the number of dimensions N and the diffusion coefficient $D_{\mathrm{i}}(t)$. Displacement of atoms in a crystal lattice will degrade the

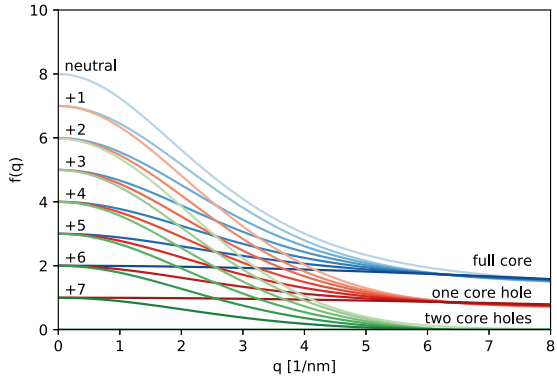

Figure 3.3. Calculated atomic form factors for the ionization states of oxygen as a function of momentum transfer $\vec{q}$ as tabulated by [61, 62]. Blue is for a K-shell with two electrons, red is for a K-shell with one core hole and green is for an empty core. Each line represents the form factor of an electronic state, and with each ionization the form factor will get lower. At very low $\vec{q}$ the scattering intensity is determined by the number of bound electrons. At high $\vec{q}$ the form factor is determined by the number of core hole electrons, and an empty core ion will not have any scattering. The intermediate region between 1 nm^{-1} and 4.5 nm^{-1} is a very important length scale for proteins and here the situation is very complex and depends on the exact details of the electronic states.

diffraction pattern. The scattering angles corresponding to high spatial frequencies are those first affected by atomic displacement. The degradation due to displacement as a function of time t and scattering vector q can be described with the following decay function [Paper I]

$$h(q,t) = e^{-4\pi^2 q^2 \sigma^2(t)}, \tag{3.8}$$

where h is in the range [0,1] and decreases with increasing q or σ. The magnitude of the scattering vector $\vec{q}$ is calculated as $q = 2sin(\theta)/\lambda$, where θ is the Bragg angle and λ is the wavelength. From this equation the similar dependence on q and σ means that the magnitude of the displacement can be directly compared to the resolution it will affect. Equation 3.8 is similar conceptually to the Debye-Waller-factor, or B-factor, that is used in crystallography to estimate resolution-dependent signal degradation due to thermal motion. See Figure 3.4 for a schematic view on how diffusion will affect the Bragg signal from a crystal.

Using Equations 3.1, 3.3 and 3.8 provided above, a full description can be made of the signal intensity when ionization and displacement is present. The intensity will be the ideal signal intensity, modified by the time integral of the factor h and k as described by

$$I_{\text{Bragg}}(\vec{q}) = r_e^2 \Delta\Omega |F_0(\vec{q})|^2 I_0 \frac{1}{T} \int_{t=0}^{T} k(q,t)h(q,t)\mathrm{d}t\,. \tag{3.9}$$

This expression is used in Paper I to calculate the expected signal from protein crystals.

To model the temporal variation in intensity during the pulse duration, the Bragg signal will be the integrated scattering over the range of the full pulse. A third factor $s(t)$ is introduced as a shape function describing the normalized distribution of intensity under the duration of the pulse. It is defined such that the full Bragg signal from an undamaged sample at scattering vector $\vec{q}$ is described by

$$I_{\text{ideal}}(\vec{q}) = r_e^2 \Delta\Omega |F_0(\vec{q})|^2 I_0 \frac{1}{T} \int_{t=0}^{T} s(t)\mathrm{d}t\,. \tag{3.10}$$

Here r_e is the classical electron radius, $\Delta\Omega$ is the solid angle of a pixel detector, $|F_0(\vec{q})|^2$ is the form factor particular for a sample [38], I_0 is the beam intensity and $s(t)$ is a function that integrates to 1. Under this ideal assumption of no damage, the Bragg signal at all angles is always directly proportional to the fluence. In a more realistic model, radiation damage will affect the Bragg signal depending on scattering angle, and the signal can be described by

$$I_{\text{Bragg}}(\vec{q}) = r_e^2 \Delta\Omega |F_0(\vec{q})|^2 I_0 \frac{1}{T} \int_{t=0}^{T} k(q,t)h(q,t)s(t)\mathrm{d}t\,. \tag{3.11}$$

This equation describes the signal I_{Bragg} from the full pulse as a function of the scattering vector $\vec{q}$. The full signal will depend on the fluence from the ex-

periment dependent term $r_e^2 \Delta\Omega |F_0(\vec{q})|^2$, the incoming intensity I_0, and is limited by the degradation caused by the ionization decay function $k(q,t)$ (Equation 3.3) and the displacement signal decay function $h(q,t)$ (Equation 3.8). The factors $k(q,t)$ and $h(q,t)$ both depend on the state of the plasma (ionization, temperature, collision rates) and changes in the plasma dynamics will affect both factors. All times t are weighted by the shape function $s(t)$, making it possible to quantify the effects of the pulse shape on the Bragg diffraction. In Paper II, Equation 3.11 is used to calculate the Bragg signal. It is important to understand that the signal on the detector will be the whole integral of the signal from the full pulse duration. Currently no detectors exist with the femtosecond time resolution required to read out only parts of the signal.

3.1.3 Modeling elastic X-ray scattering from water

Molecular dynamics (MD) simulations performed using GROMACS [64] have previously been used to study structural changes in high ionization and temperature cases [58, 65]. This approach was here complemented and expanded with ionization and heating dynamics calculated using the NLTE code to study water. The SPCE water model [66] was used, but with some modifications to allow for bonds to break. To keep track of the hydrogens after breaking, the hydrogen atom was given a radius similar to what is used in the CHARMM TIP3P water model [67]. For the non-equlibrium simulations, the oxygen-hydrogen bonds were treated as a Morse potential [68] allowing for covalent bond-breaking. The simulations were performed using periodic boundary conditions, with a constant box size and 1728 water molecules, and a starting temperature of 300 K. The ejected electrons are treated as a uniform background charge, to keep the neutrality of the simulated system.

In order to compare the simulated system with experiments, the scattered signal from water must be calculated. The radial distribution function $g(r)$ describes the distribution of pair-wise probability to find particles of types A and B the distance r apart

$$g_{\mathrm{AB}}(r) = \frac{\langle \rho_{\mathrm{B}} \rangle}{\langle \rho_{\mathrm{B}} \rangle_{\mathrm{local}}} = \frac{1}{\langle \rho_{\mathrm{B}} \rangle_{\mathrm{local}}} \frac{1}{N_A} \sum_{i \in \mathrm{A}}^{N_{\mathrm{A}}} \sum_{j \in \mathrm{B}}^{N_{\mathrm{B}}} \frac{\delta_{ij} - r}{4\pi r^2}, \tag{3.12}$$

where $\langle \rho_{\mathrm{B}} \rangle$ is the average particle density of particles with type B at a distance r around particles of type A, and $\langle \rho_{\mathrm{B}} \rangle_{\mathrm{local}}$ is a normalization using the particle B density averaged over the spherical volume with radius r around particles of type A. The structure factor $S(q,t)$ is the structure factor of the solvent calculated by taking the Fourier transform of the radial distribution function. The expected scattered signal intensity is a sum over all timesteps

$$I(q) = \frac{1}{T} \sum_{t=0}^{T} f_{\mathrm{tot}}(q,t)^2 S(q,t), \tag{3.13}$$

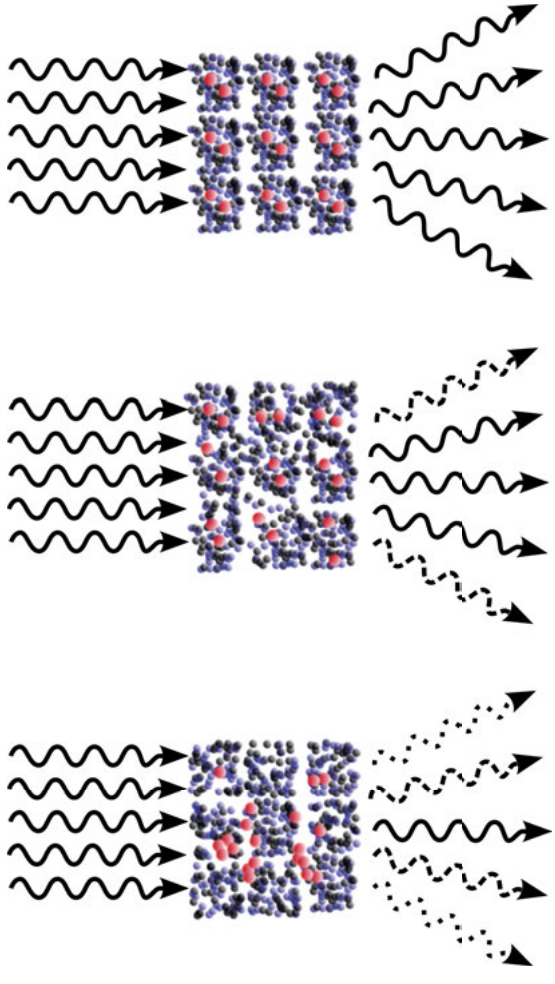

Figure 3.4. Schematic drawing on how displacement in the crystal lattice will cause a decay in Bragg signal. From top to bottom: When the crystal is intact, scattering at all angles is possible. When some displacement disturbs the lattice, the high angle scattering corresponding to high resolution will decrease. With extreme diffusion, the amplification from many crystal units is lost.

where T is the pulse duration, t is the simulation timestep and q is the momentum transfer. The total form factor $f_{\text{tot}}(q,t)$ is calculated as in Equation 3.4 using the tabulated values for oxygen. The form factor for atomic and ionized oxygen was used rather than the form factor of neutral water. This is a valid assumption since water disassociated in the simulations into oxygen and hydrogen on a femtosecond timescale under extreme intensity.

3.1.4 Photon emission from dense plasmas

The main idea in Paper VI is to use the emission from warm and dense plasmas as a fast indicator for a vetoing system in serial femtosecond experiments using a liquid jet sample delivery system. X-ray emission and absorption is modeled using the same software package as mentioned above, CRETIN. The systems investigated are experimentally relevant protein crystallography samples, either with or without protein present. The emission energy range studied was from 1eV up to 10 keV. Details about the model are presented in Section 2.4.

3.2 Experiments

Both of the presented experiments [Papers IV and V] were part of the cxi76413 beam time at the CXI instrument at LCLS [69]. Five 12-hour shifts were allocated for the experiments. Obtaining access to X-ray FEL infrastructure is highly competitive, and in this beam time researchers from 10 institutes collaborated.

3.2.1 Scattering from non-thermal heated water

Scattered light from a water jet was measured at the CXI station [69] at LCLS using the nanofocus and 6.86 keV photon energy. Purified water was injected into the experimental chamber using a gas dynamic virtual nozzle [70, 71] with a jet diameter of around 5 micrometers. The focal size of the X-ray beam was smaller, around 200 nm. The scattered light was collected on a CCD detector placed 100 mm downstream from the sample. Data was collected for all available intensities for two pulse durations, but only data from pulses with an intensity of 1.25 $\pm$0.05 mJ was analyzed. A gas energy detector was used [72] to measure the intensity of the photon pulses. Given the pulse durations of 26.3 $\pm$ 1.8 fs and 74.0 $\pm$ 1.9 fs, the fluence in the water jet was $1.35{\cdot}10^6$ J/cm^2 in both cases. The scattering at this fluence is very high and might damage the detector. An attenuator with known absorption was placed between the sample and the detector. A schematic view of the experimental setup is available in Figure 3.5. A pixel mask was applied that filtered away

shadows from the post-sample attenuator mount, pixels with fluctuations during dark measurement, and individual pixels with anomalous behavior. There are reports of non-linear detector responses at very high intensities using CCD detectors [73]. To avoid the effects from this when comparing patterns, a very narrow criterion was used: both the reported beam intensity and the measured detector intensity must fall within certain limits. The result was that only a small percentage of the patterns could be used in the analysis, only 0.1% and 2% of the shots resulted in analyzed data for the two cases. The number of analyzed patterns was 133 events for the shorter pulse and 2247 events for the longer. This may seem like low numbers given the repetition rate of 120 Hz, but the pixel detector allows for many measurements at a certain angle in a single pulse using radial averaging of many pixels from the center of the beam. The statistics for the intensity of a single q value give a standard error of less than 0.2% which gives a high level of confidence.

3.2.2 SFX of ferredoxin nanocrystals

A suspension of ferredoxin crystals was injected into the interaction vacuum chamber at the nanofocus station at CXI, LCLS, using a similar setup as above. Ferredoxin is protein that contains two iron-sulfur clusters. The beam parameters and detector configuration were as described above. Photon energies of 7.36 keV and 6.86 keV were used. The iron edge is at 7.11 keV, and it is expected that the difference between the two conditions is a more prominent ionization of iron atoms in relation to the rest of the sample above the edge. It can be noted that cross sections generally decrease with increasing photon energy, further augmenting the contrast. Comparison datasets were collected using lower intensity FEL radiation, and synchrotron radiation (described in Paper IV). Reconstruction was done with PDB structure 2FDN [75] as reference.

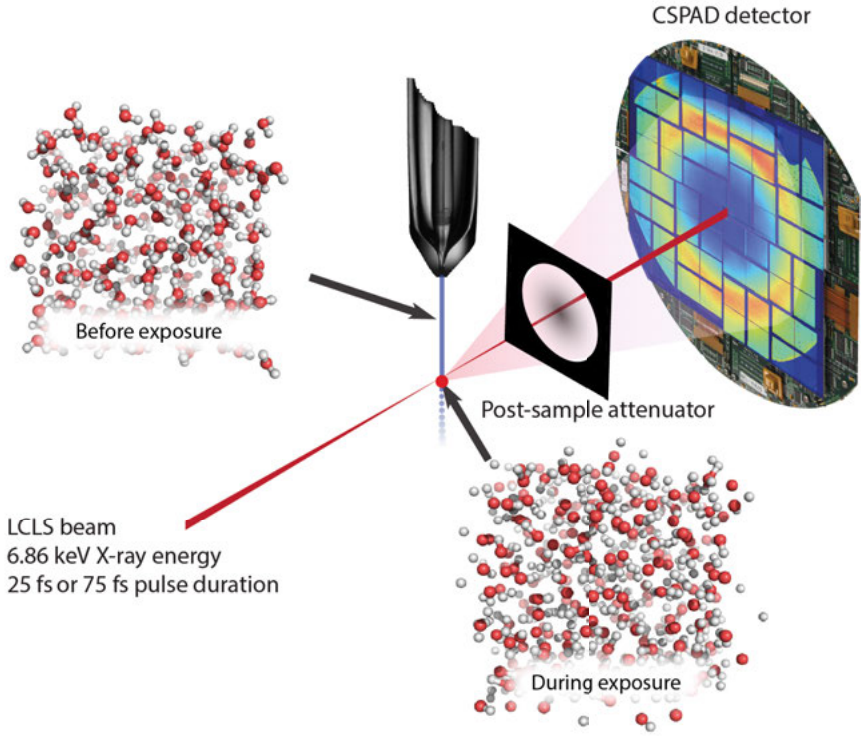

Figure 3.5. A narrow jet of room temperature water was injected using a gas dynamic virtual nozzle (GDVN) into the 200 nm X-ray focus of the CXI endstation of the LCLS. Diffraction patterns from single pulses were recorded on a CS-PAD detector with a post-sample attenuator made of a tungsten alloy film positioned downstream from the sample. The scattered signals from pulses with durations of 25 fs and 75 fs were processed and analyzed. A combination of non-local thermodynamic equilibrium modeling and molecular dynamics simulations were used to follow the dynamics of the atoms during the exposure to intense X-ray radiation. The upper left and lower right models show the state of the simulated system before and during the exposure. Broken bonds can be observed. The water transitions into a warm dense matter state during the pulse, and this transition will ultimately lead to a local explosion of the water jet [74] .

4. Results and conclusions

This chapter will go through the papers in turn, and summarize the main results and conclusions. Also shown here are a number of supplementary figures excluded from the main part of the articles that give a more in depth understanding of some of the underlying mechanisms in the studies.

4.1 Simulations of electron and structural dynamics in protein crystals (Papers I, II, III)

In order to reconstruct the electron density of the molecule, a full diffraction pattern must be collected. The elastic scattering from the sample at a certain reflection angle corresponds to a specific length scale in the sample. To model the electron distribution, all length scales up to the highest resolution at the highest reflecting angle must be collected. Each reflection from a crystal, the Bragg signal, at a certain angle relies on two properties of the sample: that the matter is periodically arranged, and that the electrons in the sample are scattering coherently. In an ideal situation, both of these properties are fulfilled and the signal will depend on the intensity of the incoming light and the size of the crystal. In reality, the sample will be affected by the measurement, and both displacement and ionization of atoms will affect the intensity of the signal.

In Papers I, II and III, NLTE plasma simulations were used to model and predict what happens in material exposed to ultrashort pulses of intense X-rays. One advantage of simulations is that many parameters can be explored, and this was used to study a range of interesting problems. The first theoretical studies estimated that pulses shorter than the onset of damage might be required to get atomic resolution data [76]. When investigated experimentally, it was shown that atomic resolution could be achieved even if the sample was undergoing changes during exposure [15]. The first paper in this thesis proposes a mechanism behind this apparent discrepancy between the initial theoretical estimates and experiments. The experiment that raised the question used protein crystals as the sample, and thus the simulation needs to model a loss in Bragg signal from a crystalline sample. To investigate this, the decay in Bragg signal due to structural dynamics in a crystal lattice and ionization of atoms is calculated for a wide range of intensities and photon energies. It is found that different mechanisms influence the signal decay depending on features of

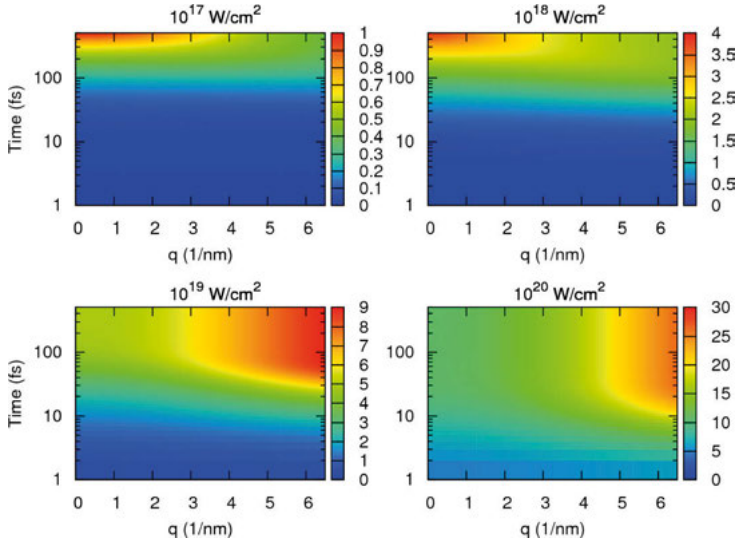

Figure 4.1. Simulation of accumulated Bragg signal from carbon atoms, as a function of time during pulse t and resolution q for different intensities. The photon energy simulated was 6 keV. The simulations are normalized by using the highest signal in the 10^{17} W/cm^2 simulation as 1 to facilitate comparison with the different cases. Note that the maximum signal for the 10^{20}W/cm^2 pulse is only 30 times higher than the maximum signal from 10^{17}W/cm^2, even though the pulse is 1000 times more intense. Reprinted from Paper I with permission from the Optical Society of America.

the incoming light. Two factors are introduced: $k(q,t)$ that describes the signal loss at momentum transfer q (corresponding to a certain spatial coherence distance in the sample) at time t due to changes in the atomic form factors due to ionization, and $h(q,t)$ that describes the signal degradation caused by displacement affecting the spatial coherence of the sample. The integral of these factors over the full pulse duration will show the intensity of the accumulated signal in relation to the ideal non-affected sample, see Figure 4.1.

An important step along the way is to calculate how much of the incoming light is absorbed by the sample. In conventional crystallography the tolerable radiation dose is around 30 MGy [14]. This would correspond to a certain number of photons hitting the sample, and gives a maximum level of signal possible for a certain sample size. The diffraction-before-destruction principle [16] predicted that much stronger signals in relation to the sample size are possible as long as the intensity is very high and the exposure is very short. To calculate the dose that the sample will absorb is not as simple as using the cross sections for cold, neutral samples. The dose rate of several GGy that is the result of such a calculation will not take into account the lowering of cross sections due to ionization. When plasma simulations are used, the estimate of absorbed dose will be more nuanced. When the incoming light is absorbed, the sample will ionize, and as a function of that the cross section for further ionization will decrease. Especially for higher intensities, the ionization cross section will be reduced due to electron loss from the atoms, leading to a reduced absorbed dose rate at the end of the pulse, see Figure 4.2. In these papers a non-linear saturation effect is predicted, where more photons added to the sample will not lead to the same ionization rate depending on the current electronic state. Due to the dynamic changes in ionization level, the concepts of maximum tolerable dose and dose rate are not as available as in synchrotron crystallography, and perhaps not as useful.

The lowered cross section for ionization goes hand in hand with a decrease in scattering cross section affecting the Bragg signal. This change is not uniform across the scattering angles, and depends on the details of the electronic state. When core electrons are removed, the scattering at high q is most affected, limiting the high resolution information from the sample. In effect, high resolution signal is cut off when the core electrons have left the atoms. At low q, the overall number of electrons is the important factor for determining the scattering power. The temperature increases during the exposure as the potential energy that comes from ionization transfers into kinetic energy. The ion temperature and the ion-ion collision rate can be calculated by the plasma model. Together they can be used to calculate a diffusion constant, and the displacement as a function of time. From the displacement estimate, the effects on the Bragg signal can be calculated. This factor is different from the Debye-Waller factor [77] used in low intensity crystallography, where more displacement in the sample will lead to a loss of signal starting at high resolution information. The factor introduced here is dynamic through the exposure.

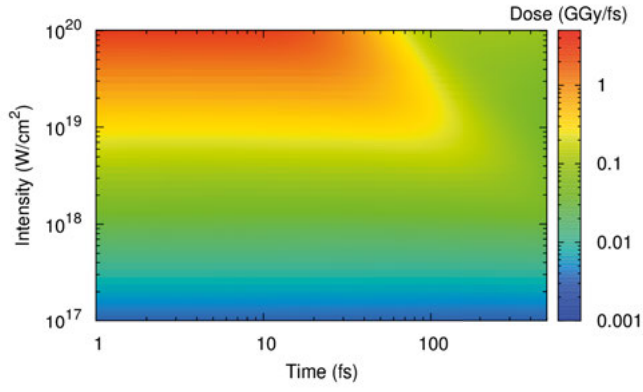

Figure 4.2. Simulation of dose rate measured in GGy/fs as a function of time during the pulse and incident intensity (photon energy is 6 keV) for photosystem I sample. At higher intensities (above 10^{19} W/cm^2), the absorbed dose rate becomes lower towards the end of the pulse as the sample becomes transparent to the incident radiation. The cause of this saturation is the ionization that lowers the cross sections for interaction between the light and the matter. Reprinted from Paper I with permission from the International Union of Crystallography.

For several simulated conditions, especially at high intensities, the ionization level is very high at the end of the pulse duration. Doubly ionized cores are not uncommon, and hence the high resolution signal will disappear within the pulse duration. The overall scattering power, especially at lower q values, is also decreasing during the pulse.

The decrease in scattering caused by structural and electronic changes is enough to cause a degradation of signal at the end of the pulse duration. In many cases this effect will reduce the signal so much that the X-ray is in fact self-gating the scattered signal, meaning that the same pulse that gives the signal also causes part of the signal to turn off. At first this may not seem desirable, but another fact must not be forgotten: more intensity will also give a stronger signal, as well as causing the self-gating earlier. For some conditions (500 fs pulse duration, 2 keV photon energy, 10^{19} W/cm^2, q=5 nm^{-1}) the effect of self-gating will be that 99% of the accumulated Bragg signal comes from the first 15% of the pulse. If this signal is enough, it simply means that some damage during the pulse duration is acceptable, which also agrees with the experiment that inspired this theoretical work. The main consideration for longer pulses than necessary is the contribution from inelastic scattering and the incoherent sample. In Paper I, an estimate of these effects is made.

From a practical point of view, very short pulse duration and very high intensity might be difficult to achieve at the same time. Simulations like this will

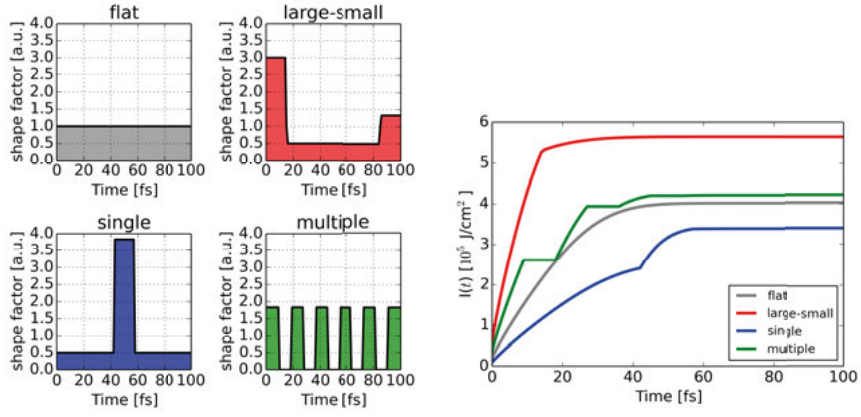

Figure 4.3. Left: Four temporal pulse shapes used in simulations. These are idealized versions of pulses from studies showing temporal pulse profile variations on a shot-to-shot basis [80, 81]. Right: The accumulated Bragg signal $I(t) = \frac{1}{T} I_0 \int_0^t k(q,t')h(q,t')s(t')\mathrm{d}t'$ as a function of time, from carbon at $q = 0.62$ Å^{-1}. A 700 nm photosystem I crystal exposed to a 100 fs long pulse, at 6 keV and intensity 2×10^6 J/cm^2 was simulated. The accumulated intensity $I(t)$ is shown in J/cm^2 and can be interpreted as an "effective" photon intensity that includes pulse shape and damage effects, and should then be used to convolute with the form factors $|F_0(q)|^2$. Reprinted from Paper II with permission from the International Union of Crystallography.

help guide the design of experiments and the choice of experimental parameters. Another future prospect is perhaps to use simulations to improve the data analysis in high intensity crystallography. If the expected decrease in signal for a certain set of conditions is known, it might be possible to compensate for this when treating experimental data. A correction factor is suggested in this article that could function as a scaling parameter for scattered signal in some scattering angles to better represent the true position of the cores, much as the Debye-Waller temperature factor is used in conventional crystallography today.

In Paper I a fixed pulse duration and temporal pulse profile was used. In Paper II the same methods are used, but the beam parameters are expanded to allow varying pulse shape in time. The signal decay for two durations is investigated, 50 fs and 100 fs. In an experimental situation the pulse profile will vary shot-to-shot [78, 79], especially for SASE beamlines. As previously established, the total signal from a sample is the time integrated signal from the sample during the full duration, and some parts of the pulse might not contribute much to the signal. Paper II used simulations to investigate the signal from varying temporal pulse profiles, photon energies and pulse intensities.

The model where the effects are separated into signal decay caused by displacement and signal decay caused by ionization allows a look into the mech-

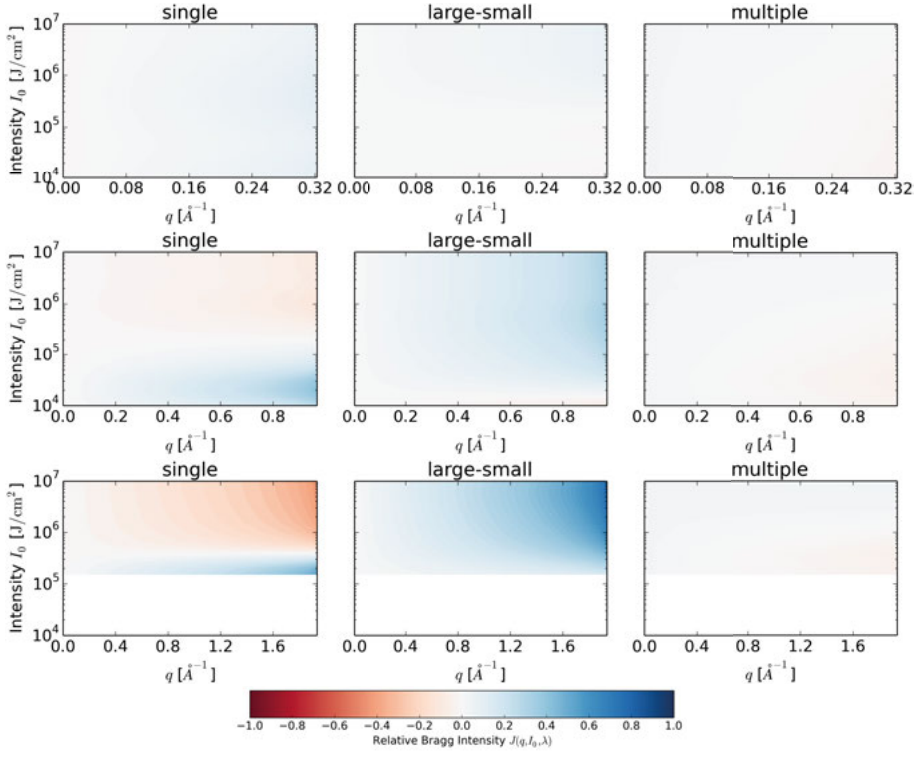

Figure 4.4. Simulation of the displacement part of the signal decay compared to a 100 fs flat top pulse as defined in Paper II. The photon energy simulated was 2 keV in the top row, 6 keV in the middle row, and 12 keV in the bottom row. It can be seen that the temporal pulse profile becomes increasingly important towards higher photon energies. Typically, the resolution dependence is strong. The formula used here is $J_{\text{Bragg}}(q,I_0,\lambda) = \frac{I_{\text{Bragg}}(q,I_0,\lambda)}{I_{\text{Bragg}}(q,I_0,\lambda)_{\text{flat}}} - 1$ with the ionization factor $k(q,t)$ omitted from I_{Bragg}. What is seen here is that at the higher photon energies, the pulse shape will affect how different scattering angles are represented depending on the intensity. This effect is explained by atomic displacements in the sample. The sample was photosystem I.

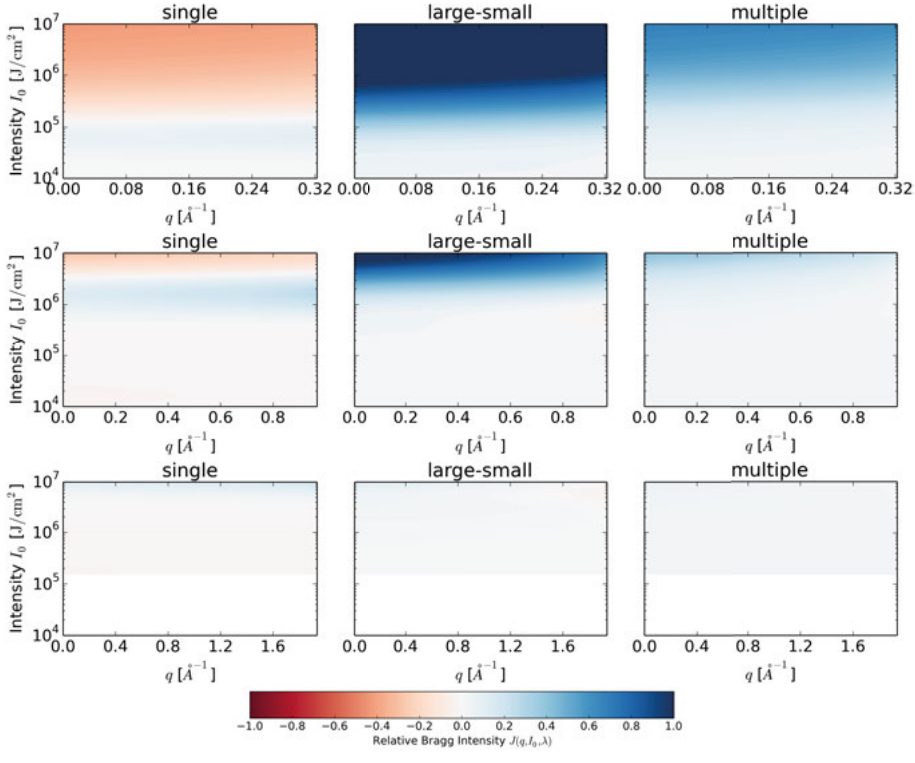

Figure 4.5. Simulation of the ionization part of the signal decay compared to a 100 fs flat top pulse as defined in Paper II. The photon energy simulated was 2 keV in the top row, 6 keV in the middle row, and 12 keV in the bottom row. The differences are more prominent at lower photon energies. Typically, the resolution dependence is weak. The formula used here is $J_{\text{Bragg}}(q,I_0,\lambda) = \frac{I_{\text{Bragg}}(q,I_0,\lambda)}{I_{\text{Bragg}}(q,I_0,\lambda)_{\text{flat}}} - 1$ with the displacement factor $h(q,t)$ omitted from I_{Bragg}. It can be seen here that when the pulse shape is varied, the overall signal will increase or decrease. This is more prominent at lower photon energies. The sample was photosystem I.

anisms at play. It is found that the temperature-driven displacement is very similar when the pulse shape is varied. The ion temperature is increasing almost linearly, and the heating rate seems to be weakly dependent on the photon flux. It is instead driven by the initial change from a neutral sample to a nanoplasma with energetic electrons present. Typically the electron temperature is very high, several hundreds of eV, and equilibration with the ions takes time. The time scale for equilibration is typically much longer than the pulse duration, on an order of picoseconds or longer. The similarity in displacement can be contrasted with the difference in electronic state between the different temporal pulse shapes. The atomic form factor is to a large extent dependent on the relation between occupancy of valence levels and core levels. This ratio is difficult to estimate as it changes dynamically during the exposure as a function of many parameters such as the ionization level, instantaneous flux, electron temperatures and processes like Auger decay.

It is clear that the trivial estimate that short and intense pulses are good still holds, high intensity will indeed always create a stronger signal, and short pulses will not allow the dynamics to disrupt the sample as much as a longer duration. The study in Paper II adds another dimension, the efficiency of adding more photons at different parts of the pulse and a resolution dependence. Late photons are gated due to the self-gating described in Paper I. A front loaded pulse will always give the strongest signal. The same number of photons with another temporal distribution will give a weaker signal, due to them arriving at a sample already affected by displacement. A few early peaks in the temporal pulse profile will start the transition into plasma without contributing much to the diffraction pattern, especially lowering the efficiency at higher resolutions. See Figure 4.3 for an example of how the accumulated signal depends on the temporal pulse profile.

In reality a FEL with SASE will have variations in the temporal pulse profile. The main conclusion from Paper II is that this will have a larger effect on some q-vectors than others for some beam parameters. The described effects are more prominent in experiments using long pulses and short wavelengths. Here high momentum transfers are affected, but the scattering representing low resolution is not as affected. This variability can be explained by Figure 4.4 that only shows the effects from displacement from three pulse profiles relative to the same number of photons in a flat pulse. Displacement effects explain the q-dependent signal variability in the high photon energy regime. The difference between pulse shapes here comes from the time at which they probe the system. This can be contrasted with lower photon energies, where ionization effects explain the difference between pulse shapes (as seen in Figure 4.5 that only shows the ionization effects), but mainly affects the overall signal strength.

To conclude, it is more important to know or control the pulse shape variability at higher photon energies if a uniform representation of scattering is required. If the temporal pulse profile can be shaped it is important not to

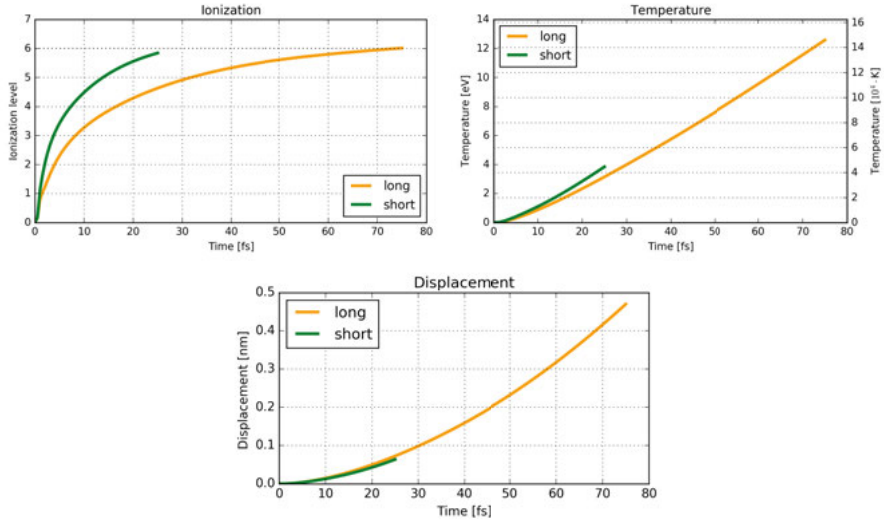

Figure 4.6. Processes in water exposed to intense X-ray pulses. Top left: Average ionization levels as calculated by NLTE simulations for pulses of 75 fs (long) duration and 25 fs (short) duration (both with a fluence of $1.35 \cdot 10^6$ J/cm^2 and 6.86 keV photon energy). The average ionization levels will within the first femtoseconds correspond to a state where each atom is ionized at least once for both simulations. It can be noted that the progress of the two simulated systems is very similar relative to their respective pulse durations, and the end states are very similar. Top right: The ion temperature increase is due to thermalization with the very hot electrons in the system. The increase rate is similar for the two simulated systems, resulting in a higher end temperature for the long pulse duration system. Bottom: Displacement calculation using equation 3.7 with temperature and collision rates from NLTE simulations. The displacement rate is very similar for the two systems, resulting in a higher end displacement for the longer pulse duration system.

forget the fact that higher intensity always gives more signal. This must be considered if there is a tradeoff between control over the pulse profile and the intensity, as is the case for seeded beams [82, 83]. The main conclusion of this article is that a sharp front is the main determining factor of the pulse shape, and gives similar results as shorter pulse durations due to self-gating effects, and a less defined front might limit the possibilities to achieve high resolution *even at high intensities*.

Preliminary measurements and estimates of the temporal profile of FEL pulses have been made [80, 84]. An alternative approach to controlling the pulse shape could be to measure it on a shot-to-shot basis, and then calculate and apply a suitable correction factor in the analysis for each diffraction pattern measured.

In Paper III a number of NLTE plasma simulations are presented in a web database. Making results and simulations available for experimentalists is in the tradition of low intensity radiation damage codes like RADDOSE [13] for protein crystallography or the photon-matter interaction database from the center for X-ray optics (CXRO) [85]. The average ionization level, the electron and ion temperatures, and a displacement estimate are presented after the user selects the beam parameters. The data available for the user will be plots similar to those presented in Figure 4.6, as well as a data file.

In the published version of the web database, the user can select from four different materials: protein crystals in solvent systems with either lysozyme or photosystem I, liquid water, or solid diamond. The main results are in line with earlier studies [Papers I and II] using the same methods, but a wider range of beam durations and samples are examined. It is seen that the photosystem I sample behaves more like pure water than the lysozyme sample in terms of temperature and ionization. This is in line with the sample composition; around 80% of the crystal is in fact water. The diamond sample has a higher density compared to protein crystals and gives higher temperatures and average ionization levels.

4.2 Localized radiation damage (Paper IV)

In Paper IV, the protein ferredoxin that contains metal cofactors was exposed to high intensity X-rays in an SFX experiment. The structure was experimentally solved using diffraction methods, and the results were complemented by plasma simulations. The protein contains twoiron-sulfur clusters that have a higher cross section for ionization than the surrounding protein. The purpose of the experiment was to investigate how this affects the perceived structure, and to understand the radiation damage mechanisms in materials with a complex elemental composition. Datasets were collected at the nanofocus station at CXI [69], LCLS using photon energy above (7.36 keV) and below (6.86 keV) the iron absorption edge using the highest available pulse energy (1.5 mJ) and 80 fs pulse durations. A higher degree of ionization can indeed be seen of the Fe atoms compared to the other atoms in the material. This is enhanced when the photon energy is above the threshold for ionization. This result is also compared to low intensity measurements at synchrotrons, also performed in the same project. In the high intensity structure measured at an FEL, the two iron-sulfur clusters differ in their perceived electron density, but in the low dose structure measured at a synchrotron the two clusters have the same type of damage. This suggests that the geometry and the local bonding will affect the degree of ionization.

The NLTE plasma model is used here to explain the absorption and ionization dynamics over time for the elements carbon, sulfur and iron. The ionization for carbon is almost saturated after 15–20 fs, but the heavier elements

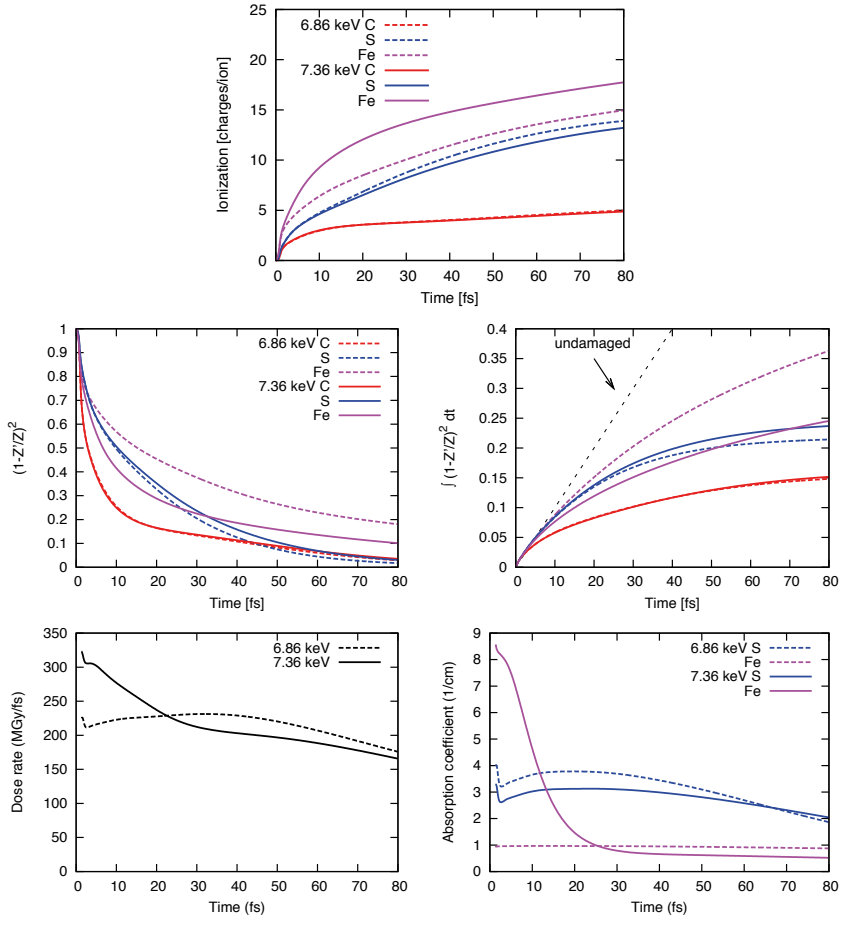

Figure 4.7. Ionization dynamics simulated with the plasma code CRETIN. Top: Average ionization per C, S and Fe atoms, as a function of time during the pulse, for two photon energies (6.86 keV and 7.36 keV). Ionization saturates faster for light atoms. For Fe it is dominated by collisional ionization. Middle left: Scattering power for C, S and Fe ions as a function of time, estimated from the number of bound electrons (without atomic form factors). Middle right: Expected accumulated signal during the pulse due to the loss of scattering power for C, S and Fe ions, compared with the neutral undamaged atoms (black dashed line). Bottom left: Calculated dose rate (MGy/fs) in the sample as a function of time, for two photon energies. The dose rate decreases during exposure due to saturation in ionization and changes in the photoionization cross sections. Bottom right: Absorption coefficient for Fe and S in the sample as a function of time. The drastic change in absorption for Fe above the K-edge in the first 20 fs is due to a rapid loss of electrons and a lowering of the ionization potential in the plasma environment. Reprinted from Paper IV with permission from the International Union of Crystallography.

continue to ionize during the full pulse duration. Even for iron, the main ionization mechanism is collisional ionization that affects the valence electrons. The difference below and above the iron absorption edge manifests as a steep decrease in absorption coefficient for the higher photon energy. The absorbed dose rate starts at around 300 MGy/fs but decreases down to 200 MGy/fs after 25 fs. For the lower photon energy case the dose rate is around 200 MGy/fs during the whole pulse. The consequence of this is that the scattering power decreases more rapidly for the case above the iron edge, and the total scattering is lower. See Figure 4.7 for a description of element-wise ionization levels, scattering power, accumulated signal, dose rate and absorption coefficient as a function of time during the pulse. All of these can only be accessed as global parameters within a simulated zone. Effects originating from local geometry and bonds were not simulated, and would require a more elaborate model.

The plasma modeling predicted the overall ionization behavior seen in the reconstructed data, but the geometrical and bonding effects are beyond the scope of a continuum model. Local or specific damage is defined as damage only affecting a certain atom, bond or region, in contrast to global damage that either affects the whole structure or a certain resolution. This experiment shows that local damage can happen at FEL measurements, and to determine the structural effects more detailed modeling is required. The changes in reconstructed electron density could be partially attributed to changes in scattering power, and this effect can be predicted by the current model.

4.3 Non-thermal heating of water (Paper V)

Water is almost always present when biological samples are investigated with FEL-based methods. Currently the main sample delivery method for protein crystals is a water jet. Paper V shows experimentally for the first time that the water itself undergoes ultrafast structural changes during the exposure. Scattering from a water jet was investigated at the CXI station at LCLS. A rather high fluence is used, $1.35 \cdot 10^6 \mathrm{J/cm}^2$, and the photon energy was 6.68 keV. Pulses with durations of 25 fs and 75 fs were used. It was experimentally challenging to have the same intensity on the sample for different pulse durations, and both the setup of the experiment and post-processing filtering were used to make sure that only the effects from changed duration was investigated. A change in diffraction at the higher scattering angles was observed. This result is important from a purely experimentalist point of view, as the background is often subtracted to reveal Bragg spots in crystallography. The implication is that background compensation should be done dynamically as the water background will not be static under different conditions. Similar effects may be seen in any amorphous material at these intensities.

When the study is complemented by simulations, the conclusion is that the changes are due to structural dynamics in the sample. In Figure 4.8 the exper-

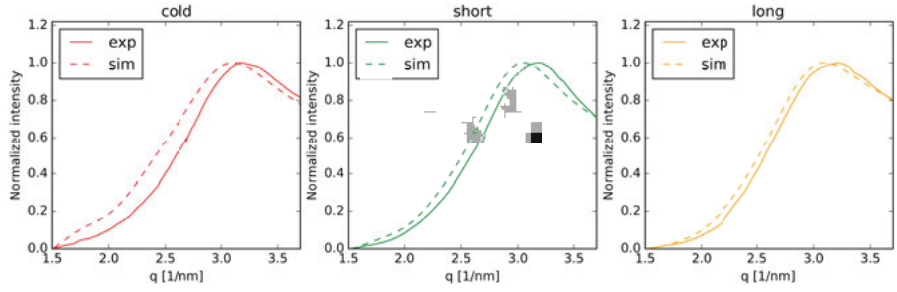

Figure 4.8. Direct comparison of scattering intensities as a function of scattering vector, $q = 2\sin(\theta)/\lambda$, for experiments and simulations. Left: Conventional in-house X-ray source on a water droplet compared to molecular dynamics simulation of 300 K water. Middle and right: XFEL pulse of 25 fs (short) duration and 75 fs (long) duration (both with a fluence of $1.35{\cdot}10^6$ J/cm^2 and 6.86 keV photon energy) compared with MD and NLTE simulations, calculated from the O-O radial distribution function and the electronic states of the system. The X-ray parameters in the simulations are chosen to match the experimental ones. The curves are normalized to the maximum of the peak with the minimum subtracted.

imental scattering intensity is shown compared to the simulated intensity. To see side by side comparisons of the measured scattering intensity as a function of scattering angle for the two pulse durations, see Paper V. Figure 4.6 gives an early indication of the underlying processes; the temperature in the sample is expected to increase in a similar manner in relation to the absolute time, but the ionization increases in relation to the integrated photon flux. When using a simple diffusion model that takes temperatures and collision rates into account, we see that the diffusion rate is very similar in the two cases, but the longer duration allows a longer progress. On the other hand, the electronic state stays very similar for the two cases when at the same fraction of the full pulse duration.

To investigate the dynamics of the structural changes, a hybrid model including molecular dynamics was used to investigate the signal from a sample undergoing changes. This allows for a detailed look into how the bonds break in water exposed to high-intensity X-ray radiation. The radial distribution function (RDF) shows that the coordination beyond the first solvation shell disappears on a timescale of around 20–30 fs. Figure 4.9 illustrates how the RDF and the structure factor changes in time during the exposure.

It is found that the time evolution of the electronic state is very similar for the two systems, and mainly affects when the system is probed by the X-rays. In both cases the ionization-driven decrease in atomic form factors will gate much of the signal from the end of the pulse. In the 75 fs pulse case, we still see scattering from a sample that has undergone a phase transition into plasma. This is further supported by Figure 4.10. It is clear that a non-

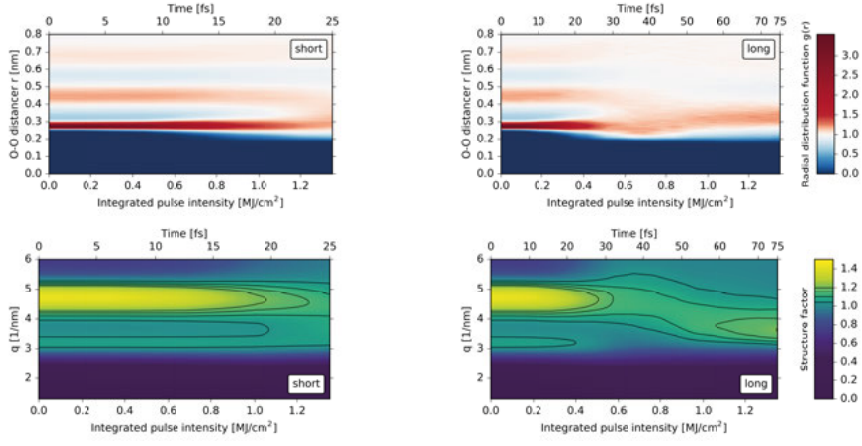

Figure 4.9. Top: Simulated time evolution of the radial distribution function (RDF) of water during the X-ray pulse (6.86 keV photon energy), shown as a function of integrated intensity for the two pulses. The short (25 fs) and long (75 fs) pulses have the same total intensity. In both cases, the structure of water does not appear to change until roughly 20 fs. Bottom: Time evolution of the structure factor, calculated from the RDF above. The experimental measurements were made from 1.5 to 3.7 nm^{-1}.

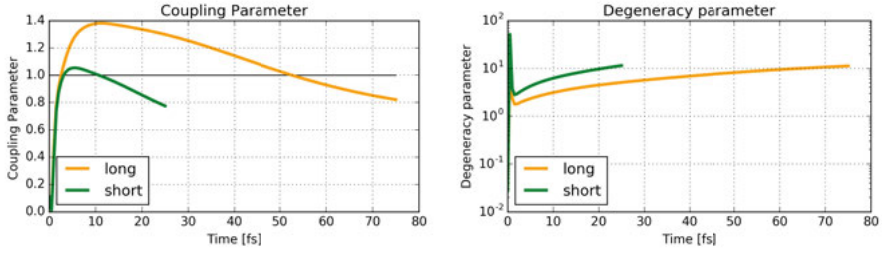

Figure 4.10. Left: The plasma coupling parameter as calculated by NLTE simulations for pulses of 75 fs duration and 25 fs duration (both with a fluence of $1.35 \cdot 10^6$ J/cm^2 and 6.86 keV photon energy). Within 1–2 fs the system will leave the regime that allows liquids and enter the warm dense matter regime. Right: The degeneracy parameter for pulses of 75 fs duration and 25 fs duration. This parameter is >1, implying that statistical modeling can be used instead of a quantum treatment.

thermal, ionization-driven heating process has occurred. When comparing the experiments and the simulations (see Figure 4.8) it is seen that the trends from experiments can be reproduced using the model.

In summary, we observe for the first time structural changes in water due to a non-thermal heating process leading to a phase transition into warm dense matter. Measuring these changes gives us insights into the conditions during SFX experiments using liquids as a delivery system, in addition to the fundamental research of ultrafast dynamics.

4.4 Photon plasma emission from protein samples (Paper VI)

The high repetition rates of new FEL sources provide new opportunities and challenges. The repetition rate at LCLS is currently around 120 Hz, but the European XFEL will have a repetition rate of 27 000 pulses per second. The amount of data produced will be very high, and it is likely that not all diffraction data can be read out from the pixel detectors [86]. Until a system is in place that can save all data produced, many useful diffraction patterns will be thrown away without being analyzed. On the other hand, not all pulses will hit a protein crystal, and instead only produce scattering from the sample delivery liquid.

Paper VI presents an idea for a physical process that can be utilized for a vetoing system in hit-finding. Photon emission from the nanoplasma of sample either with or without proteins was compared using NLTE plasma simulations. It is found that the spectrum varies not only with sample composition, but also with beam parameters, making a trivial discrimination difficult. This is especially apparent in the XUV region where black body radiation will be a very significant factor in the total emitted radiation. The pulse to pulse variation in intensity will likely create a variation in this region on the same order of magnitude as the differences between elemental compositions. In this energy region not only the carbon and nitrogen from proteins will emit photons, but also the oxygen from both protein and surrounding water.

The characteristic line emission in the hard-X-ray region above 1 keV is better suited, especially emission from the heavier elements emitting photons at energies well above the black body radiation using moderate intensities. Figure 4.11 depicts the spectrum from photosystem I crystals in a delivery liquid. The sulfur emission at around 2.3 keV is a good candidate for a hit reporter unique to proteins. From an experimental point of view the presence of buffers and carrier liquids must also be considered. Depending on the protein, almost all elements inside the protein can be also be used either in the crystallization process or as a stabilizing buffer, including sulfur. In that case there will be no unique element to identify a protein hit. A scheme substituting the sulfur in methionine for selenium is suggested, as the emission from

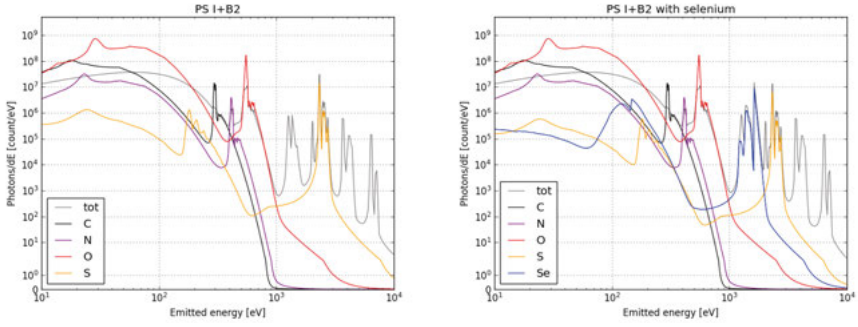

Figure 4.11. Total spectra from the sample and emission spectra for different elements. The element spectra are from the middle of the sample only. The total signal includes absorption effects from the sample as the signal goes through. Simulations were done with 10^{19}W/cm^2. From left to right, samples are photosystem I (PS I+B2) and photosystem I where the methionine sulfurs have been exchanged for selenium. Above 1 keV, the heavier elements have emission lines beyond the blackbody background (the temperature is the same for all ions). The selenium substitution shows the possibility to biochemically add new spectral features, with selenium (in blue) different than sulfur (in yellow). Note that the scale is in emitted photons per energy unit, to emphasize that the emitted number of photons at high energy could be considerable. Reprinted from Paper VI with permission from the International Union of Crystallography.

Se will be in a unique region free from emission from most other commonly used elements for buffers or delivery liquids.

The photon emission in the hard X-ray regime has many features depending on the elemental composition and the beam parameters. In Figure 4.12 emission in this region is shown as a function of time. There will be shifts in the emission due to continuum lowering, and many of the processes will continue after the incoming pulse, creating an afterglow well after the end of the pulse duration.

The regions with emission unique for proteins are good candidates for simple detectors with a limited bandwidth that will only count photons without any intention of resolving different energies as an experimental result. For other applications the actual spectral information may be interesting, and here the afterglow must be considered. Diffraction-before-destruction is possible using ultrashort pulses, but "Spectroscopy-before-destruction" may not always be possible for spontaneous processes in warm dense matter. The sample will stay in the interaction region as a nanoplasma and many processes will continue well after the pulse has ended.

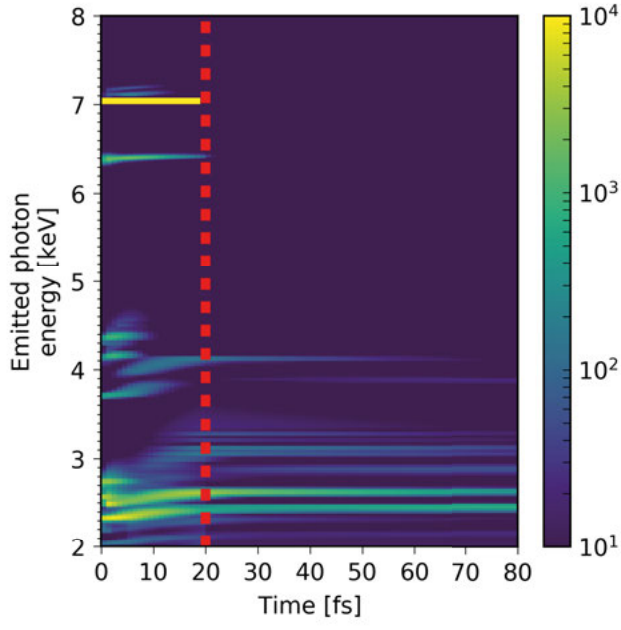

Figure 4.12. Photon emission spectra as a function of time. The sample simulated is photosystem I exposed to 10^{19}W/cm^2 fluence 20 fs duration pulse with 7keV photon energy. The pulse end time is marked with a red dashed line. The most prominent lines at 2.3 keV and 2.5 keV are K-alpha and K-beta emission from sulfur. Note the small shifts that are the result of the continuum lowering. Calcium and iron are also present in this sample, and the emission lines from those can also be seen. Much of the emission will in general come after the pulse has passed the sample, and all current detection methods will measure the sum of all radiation.

5. Outlook

The use of high intensity, short pulse duration X-ray sources for structural biology has during the last decade gone from proof-of-principle experiments to being an established method. For the last couple of years, SFX has been used to solve the atomic structure of several important proteins, and it has also been shown that the method is suited for time-resolved studies [34, 28, 87]. It was listed as one of the ten most important breakthroughs of the year in 2012 by the journal Science [88], and it is fair to say that the method is a great success.

This thesis is part of a larger effort to explain the processes that are important to get good results, and to further improve the experiments. It has been shown that the formation of small nanoplasmas within the duration of the beam may not always be a problem for imaging and obtaining a structure [Papers I and II], and perhaps even be used to improve the efficiency of experiments [Paper VI]. For the first time local damage at high intensities is shown [Paper IV], and ultrafast structural changes in water during a timescale of tens of femtoseconds is demonstrated [Paper V]. Different conditions for experiments are mapped, and tools are provided to users for experimental planning [Paper III].

Several of the papers predict effects that are yet to be investigated, that could be utilized to make experiments more efficient. To test the hit-finding scheme proposed in Paper VI, photon emission from varying samples must be measured, and further studies can include the constraints from realistic detectors.

It would be very interesting to extend the work on temporal pulse profiles [Paper II] with the correction factors from Paper I combined with an experimental measurement of the pulse profiles on a shot-to-shot basis. It is likely that more of the experimental data could be analyzed and used if the variations in the datasets for certain Bragg spots are explained, instead of being thrown away as noise. The suggested correction factors introduced in Paper I may be introduced into the database presented in Paper III and made easily available to the XFEL users. This would allow the community to take radiation damage into account when doing reconstruction.

Interplay between modeling and experiments is required to understand the physical processes in the ultrafast high intensity regime. In Paper V, the study on ultrafast structural changes in water, the modeling was greatly improved by the new challenges provided by experimental results, and to understand the signal a hybrid model had to be developed. To test that model further, experiments are needed. When fully understood, the structural changes observed

in delivery liquids can serve as an ultrafast thermometer on the femtosecond timescale.

Our picture of interaction dynamics is not complete until the actual diffraction pattern can be calculated and the electron map from a sample undergoing dynamics can be modeled. Ideally this would then be compared to experiments in order to refine the modeling, and understand the mechanisms in crystallography experiments better.

Some steps in the simulation methods presented in this thesis can certainly be expanded with more details. Currently instant thermalization of electrons is assumed and used in the model. There have been attempts to simulate and predict how a non-equilibrated electron distribution would affect this assumption [47]. Many of the equations used in the code will then have to be updated to allow for a distribution of electron energies instead of the more established temperature measurement. From the crystallography article [Paper IV] investigating local damage it is clear that some effects are impossible to predict without more refined models than those currently in use. The differences in the two FeS sites show that an understanding of local changes is required. The methods used in this thesis are good for global changes in how different resolutions are affected, but bonds and geometry are not possible to simulate for complicated systems at the moment. The approach used in Paper V for a water system requires extensive work to be usable for a complex protein environment, and effects such as excitations are not included in the basic MD-models.

The first generations of X-ray FELs have seen the development of longer and more expensive facilities; the European XFEL is housed in 3.4 km long tunnel that spans two states, and cost 1.22 billion euros. Will we see even higher intensities, even longer and more expensive infrastructure in the next generation? So far, higher intensity is needed when the sample size is going down. Single particle imaging using single proteins with atomic resolution will, if demonstrated, be one of the biggest achievements of the century. The possibilities opened up by the ability to collect a full structural dataset from a handful of actual protein molecules, without complicated sample preparation, are enormous and can not be overestimated.

The possibilities opened up along the way towards single protein imaging have so far proved to be methods in their own right. It is likely that more specialized facilities and beamlines will be constructed and used, depending on the needs of the experiments. Maybe new methods will be demonstrated that will allow high intensity studies in home-labs? One interesting development is that methods from the high intensity SFX experiments are being adapted to low intensity synchrotron experiments. One example is Paper XI, where a new tape drive is used together with microfluidic mixing to get a serial crystallography setup at a synchrotron beamline. This proof-of-principle paper shows the possibility to study enzyme structural dynamics at synchrotrons with very low sample consumption.

Recent ideas rely on the incoherent emission to create diffraction using protein crystals [44]. Paper VI shows that plasma processes might be important to consider when designing such experiments, especially when utilizing short pulses. One concern is that the afterglow in emission after the end of the pulse seen in the simulations might interfere with experiments that rely on very short bursts of emission on the same time scale as the X-ray pulses.

Many of the SFX studies done to date have relied on the fact that the sample comes in large amounts. A significant share of all sample consumed during a beamtime will not be intercepted by a pulse, and it is even likely that good data will be thrown away without analysis due to slow readout from the detectors in the high repetition rate facilities. With the difficulties of getting access to infrastructure, and the future need to be able to use rarer samples, it will become more and more important to get as much knowledge as possible out of an experiment. The results and ideas presented here are part of this endeavour. The future in using X-rays for structural determination is bright!

6. Author contributions

The articles presented here are the work of many persons, as indicated by the sometimes long author lists. To specify my contributions:

Paper I: Participated in discussions and writing, constructed a new pipeline for algorithms to cross check data analysis.

Paper II: Main contributor to simulations, analysis, discussions, coordination and writing.

Paper III: Participated in discussions and writing. Main contributor to plasma simulations and analysis code.

Paper IV: Participated in discussions, FEL experiment and writing. Performed plasma simulations and analysis.

Paper V: Performed the experiment, analyzed the experimental data and simulations, discussions and writing. Main contributor to plasma simulations and analysis.

Paper VI: Responsible for designing the study, simulations and analysis, discussions and writing.

7. Svensk sammanfattning

Ljus med olika våglängder används i många av de vanligaste metoderna för att studera materia. När man vill undersöka mycket små objekt, exempelvis de makromolekyler som är viktiga inom biologin, krävs ljus med mycket kortare våglängd än för synligt ljus. Om man vill uppnå atomär upplösning krävs en strålning med ungefär samma våglängd som de interatomära avstånden, vilket innebär att man behöver röntgenstrålning. Under de senaste 60 åren har man kunnat bestämma strukturen hos över 100000 proteiner med hjälp av röntgenljus från en typ av strålkälla som kallas synkrotroner, och fler tillkommer varje dag. De flesta av dessa har bestämts med hjälp av metoden röntgenkristallografi, där man utifrån analys av spridningsmönstret kan räkna ut strukturen av ett material som träffas av röntgenstrålning. Spridningen från ett enskilt protein är mycket svag, och istället för att studera enskilda proteinmolekyler har man studerat kristaller. I en proteinkristall finns en upprepning, en spatiell koherens, som förstärker spridningen i vissa vinklar. När man studerar spridningen av ljuset från en kristall ser man ett diffraktionsmönster med punkter med hög intensitet, Bragg-punkter. Genom en rekonstruktionsprocess kan man beräkna hur materian som spred ljuset såg ut, där man mäter hur mycket ljus som spridits i olika riktningar. Alla riktningar är viktiga för att få en bild av provet, och de högre vinklarna ger information om de minsta detaljerna.

Det finns en gräns för hur små kristaller man kan studera med en synkrotron. Signalen är svagare från en liten kristall, och om man utsätter den för ljus under mycket lång tid kommer ljusets interaktion att leda till strålskada och påverka provet. Det finns också en gräns för hur stora kristaller man kan producera av vissa viktiga typer av proteiner. Sammantaget ger detta ett stort behov av komplementära metoder.

Röntgenlaser är en relativt ny typ av strålkälla som har funnits tillgänglig i cirka ett årtionde. I en röntgenlaser kan extremt intensiva pulser som är några tiotals femtosekunder långa framställas. Redan innan de togs i bruk förutsågs de ha egenskaper som gör det möjligt att studera biologiska molekyler. Även om provet kommer att omvandlas till plasma och förstöras av strålningen så har pulsen redan passerat provet innan det påverkar själva mätningen. Denna princip har sedan testats i verkligheten och är på väg att bli en etablerad metod.

Denna avhandling berör den ljus-materia-interaktion som sker i röntgenlaserexperiment. De sex artiklar som presenteras har sin kärna i experiment och simuleringar av hur röntgenstrålning interagerar med ett plasma.

Den första artikeln beskriver en modell som från beräknade joniseringsprocesser, elektroniskt tillstånd och temperaturer beräknar en Bragg-signal för

ett prov som exponeras för en intensiv röntgenpuls. Det förutsägs att joniseringen är så hög att en stor del av strålningen kommer att passera provet utan interaktion, vilket leder till ett icke-linjärt samband mellan intensitet och signal. Diffusion orsakad av uppvärmning kommer att störa signalen, särskilt vid höga spridningsvinklar som representerar information med kort spatiell våglängd, det vill säga den som behövs för att få hög upplösning. Samverkan mellan de olika processerna är sådan att vissa Bragg-punkter kommer att sluta ge signal under pulsens gång. Oväntat långa pulser kan användas utan att ett skadat system avbildas, då de senare delarna från ett system som går sönder inte kommer att ge signal.

Den andra artikeln utvidgar metoderna från den första till att också gälla pulser som är oregelbundna i tiden. I en verklig röntgenlaseranläggning kommer pulsformen att variera från puls till puls, och arbetet som presenteras här undersöker konsekvenserna av detta. Det visar sig att en pulsformsvariation påverkar hur jämn signalen är från olika längdskalor.

När avbildningstekniken mognar så ökar behovet av snabb referensinformation inför experimentplanering. Ett antal standardfall av strålning-materia-interaktion har undersökts och publicerats i en databas som är tillgänglig via internet. Den tredje artikeln presenterar denna databas, där användaren kan få tillgång till simuleringsresultat om jonisering, temperatur och diffusion i olika prov som interagerar med intensiv röntgenstrålning.

Den fjärde artikeln behandlar lokal strålskada i proteinet ferredoxin, och jämför experiment från en synkrotron med experiment som använder röntgenlaser. Simuleringar används här för att beskriva hur mycket energi som provet absorberar, och den totala joniseringsnivån. Hälften av alla proteiner har någon typ av metallatomer i sin struktur. Tvärsnittet för jonisering är mycket högre för dessa, och man har därför ofta observerat att dessa proteiner är svåra att strukturbestämma med hjälp av synktrotroner på grund av strålskada. Experimenten visar att den lokala skadan i ferredoxin är olika beroende på om synkrotronstrålning eller röntgenlaser använts.

Den femte artikeln utvidgar analysen av diffusion. Genom att beräkna hur individuella molekyler rör sig (molekyldynamik), kan mer materialspecifik information fås fram om hur signaler påverkas. Beräkningarna kompletteras med en experimentell studie från röntgenlasern LCLS. Studien visar experimentellt att vatten genomgår strukturella förändringar under pulser mellan 25 och 75 femtosekunder. Pulser med samma antal fotoner men med olika längd skickas mot en vattenstråle, vars spridningsmönster detekteras. Simuleringarna visar att förklaringen är en icke-termisk uppvärmning driven av jonisering, där det sker en uppvärmning från rumstemperatur till hundratusen grader under röntgenpulsen. Skillnaderna i spridning mellan de två fallen förklaras av en strukturell förändring när bindningarna i vattenmolekylerna bryts.

De nya strålkällornas höga pulsfrekvens ställer höga krav på lagring och processning av data. Förmodligen kommer man inte hinna att processa all experimentell data som samlas in, utan slumpmässigt tvingas spara data och

hoppas på att man sparar information från pulser som innehåller intressant information. I den sjätte artikeln undersöks hur röntgenemission från ett varmt plasma kan användas för att skilja på prov som innehåller protein och sådana som bara innehåller vatten eller andra vätskor. Det visar sig att svartkroppsstrålning, den process som gör att varma material glöder, ger stark strålning som sträcker sig långt upp i röntgenområdet. Signalen från de lätta grundämnen som förekommer i proteiner blir då svår att skilja från bakgrunden. Signalen från karaktäristisk linjeemission föreslås som alternativ. Om man väljer bort den data som saknar den signalen, kommer man kunna få mycket effektivare datainsamling. Ett viktigt delresultat är att emissionen från ett plasma fortsätter långt efter att den ursprungliga röntgenpulsen passerat.

Sammanfattningsvis berör detta arbete ultrasnabba fenomen i materia som utsätts för intensiv strålning. Genom att studera och förstå dessa processer kan man förbättra effektiviteten i röntgenlaserexperiment.

8. Acknowledgements

Of all the things that I have to do to get a PhD, forgetting to put someone important to me in the Acknowledgements section is the thing that scares me the most. If you don't find your own name here, that doesn't mean that I am not grateful for meeting you. In fact, you can find a personal dedication written inside the front cover!

Calle, thank you for not only doing the supervisor duties (believing in me even when I didn't, pushing me in the right direction, reading my texts, coming with snacks close to deadlines, discussing electrons over a beer etc.), but also for being a very good friend. Doing a PhD takes a long time, and these five years would have been very different without the fantastic discussions we have had about things big and small in life.

Nic, thank you for becoming part of the supervision team, not only as a guide to the weird world of plasmas, but also for always being there both literally and figuratively. Working with you have always been great fun. As you say: "We keep in touch".

Olle, thank you for being the stealthy co-supervisor asking interesting questions that many times have led me right.

To be able to perform this kind of research you need very good infrastaructure. I would like to acknowledge LCLS at Stanford Linear Accelerator Center (SLAC), FLASH and Petra III at Deutsches Elektronen-Synchrotron (DESY) in Hamburg, MAXlab III in Lund, and Fermi in Trieste for access to the facilities needed for the work presented here.

Computer clusters were heaviliy used in this research. I have used the resources from Uppsala multidisciplinary center for advanced computational science (UPPMAX) and the daVinci cluster hosted at the laboratory of molecular biophysics.

Stiftelsen för strategisk forskning (SSF), Wallenbergs resestipendium, Liljevalchs resestipendium, Volkswagen Stiftung, Stiftelsen för internationalisering av högre utbildning och forskning (STINT) and stiftelsen ÅForsk have all made this research possible through generous funds.

Clara and Chris, thanks for all the fun we have had in the group. I am looking forward to seeing what you will do next!

Davide, Torsten and Ieva for introducing me to the first office to the left in the corridor, and Geethanjali, Nicklas and Delphine for sharing it with me.

I didn't do my undergraduate education in physics, but I am very happy to have met all the people in the division of molecular and condensed matter physics.

There are some people at the department that have done more than what they had to in their roles, and this has meant a lot to me. Inger, Åsa and Håkan have all in various ways made this thesis possible.

I must thank my fantastic collaborators and co-authors from the BMC biophysics group (where I started in the field with a project work in 2009), from the CFEL and EUXFEL groups in Hamburg (where I always have felt welcome), from the Max Planck institute in Heidelberg, from the ELI Beamlines in Prague and from Arizona State University and many other places. It has been great fun to explore the world of short intense pulses together, and I hope that we will continue to meet for many years to come. I want to especially thank Ken for your hard work with the water diffraction, Howard for your expertise in plasma simulations, Andy and Anton for your experimental skills, and finally Henry for always adding the extra touch.

During the last two years, I have also been involved in some new projects. In these I have worked with many fantastic people, but I would like to especially mention Dominik, Stephan, Tom and Rick.

Thanks to everyone who did their PhD before me, and helped me realize that this is something that I can do too. Thanks to all the fantastic teachers, mentors and students that I have met throughout the years.

I am lucky to have many friends, both within the scientific field and outside. I have had a lot of fun during these years at conferences, road trips, workshops, game nights, pub evenings, while listening to or creating music, while climbing walls, eating food, drinking coffee, talking, walking, celebrating small or big events, close by or in other places in the world.

Till slut vill jag tacka min fantastiska släkt i Västerås, Köping, Hällberga,
Nora, Stockholm, Uppsala, Umeå och Hayward.
Mina föräldrar och min syster har
varit med på hela resan.
Christine för allt.
Tack!

References

[1] J. C. Kendrew, G. Bodo, H. M. Dintiz, R. G. Parrish, H. Wyckoff, D. C. Phillips, A three-dimensional model of the myoglobin molecule obtained by x-ray analysis, Nature 181 (4610) (1958) 662–666.

[2] S. Furberg, On the structure of nucleic acids, Acta chem. scand 6 (1952) 634–640.

[3] J. D. Watson, F. H. C. Crick, Molecular structure of nucleic acids: A structure for deoxyribose nucleic acid, Nature 171 (4356) (1953) 737–738.

[4] M. H. F. Wilkins, A. R. Stokes, H. R. Wilson, Molecular structure of nucleic acids: molecular structure of deoxypentose nucleic acids, Nature 171 (4356) (1953) 738–740.

[5] R. E. Franklin, R. G. Gosling, Molecular structure of nucleic acids: molecular configuration in sodium thymonucleate, Nature 171 (4356) (1953) 740–741.

[6] F. Sanger, H. Tuppy, The amino-acid sequence in the phenylalanyl chain of insulin. 2. The investigation of peptides from enzymic hydrolysates, Biochemical Journal 49 (4) (1951) 481–490.

[7] Principles and techniques of biochemistry and molecular biology, 6th Edition, Cambridge University Press, Cambridge ; New York, 2005.

[8] J. Drews, Drug Discovery: A Historical Perspective, Science 287 (5460) (2000) 1960–1964.

[9] R. M. Bill, P. J. F. Henderson, S. Iwata, E. R. S. Kunji, H. Michel, R. Neutze, S. Newstead, B. Poolman, C. G. Tate, H. Vogel, Overcoming barriers to membrane protein structure determination, Nature Biotechnology 29 (4) (2011) 335–340.

[10] RCSB PDB - SCOP Browser (Oct. 2013).

[11] C. Blake, D. Phillips, Effects of X-irradiation on single crystals of myoglobin, in: Proceedings of the Symposium on the Biological Effects of Ionizing Radiation at the Molecular Level, International Atomic Energy Agency, Brno, 1962, pp. 183–191.

[12] R. J. Southworth-Davies, M. A. Medina, I. Carmichael, E. F. Garman, Observation of decreased radiation damage at higher dose rates in room temperature protein crystallography, Structure 15 (12) (2007) 1531–1541.

[13] O. B. Zeldin, M. Gerstel, E. F. Garman, RADDOSE-3d : time- and space-resolved modelling of dose in macromolecular crystallography, Journal of Applied Crystallography 46 (4) (2013) 1225–1230.

[14] J. M. Holton, A beginner's guide to radiation damage, Journal of Synchrotron Radiation 16 (2) (2009) 133–142.

[15] A. Barty, C. Caleman, A. Aquila, N. Timneanu, L. Lomb, T. A. White, J. Andreasson, D. Arnlund, S. Bajt, T. R. M. Barends, M. Barthelmess, M. J. Bogan, C. Bostedt, J. D. Bozek, R. Coffee, N. Coppola, J. Davidsson, D. P. DePonte, R. B. Doak, T. Ekeberg, V. Elser, S. W. Epp, B. Erk, H. Fleckenstein,

L. Foucar, P. Fromme, H. Graafsma, L. Gumprecht, J. Hajdu, C. Y. Hampton, R. Hartmann, A. Hartmann, G. Hauser, H. Hirsemann, P. Holl, M. S. Hunter, L. Johansson, S. Kassemeyer, N. Kimmel, R. A. Kirian, M. Liang, F. R. N. C. Maia, E. Malmerberg, S. Marchesini, A. V. Martin, K. Nass, R. Neutze, C. Reich, D. Rolles, B. Rudek, A. Rudenko, H. Scott, I. Schlichting, J. Schulz, M. M. Seibert, R. L. Shoeman, R. G. Sierra, H. Soltau, J. C. H. Spence, F. Stellato, S. Stern, L. Strüder, J. Ullrich, X. Wang, G. Weidenspointner, U. Weierstall, C. B. Wunderer, H. N. Chapman, Self-terminating diffraction gates femtosecond X-ray nanocrystallography measurements, Nature Photonics 6 (1) (2011) 35–40.

[16] R. Neutze, R. Wouts, D. van der Spoel, E. Weckert, J. Hajdu, Potential for biomolecular imaging with femtosecond X-ray pulses, Nature 406 (2000) 752–757.

[17] D. A. G. Deacon, L. R. Elias, J. M. J. Madey, G. J. Ramian, H. A. Schwettman, T. I. Smith, First operation of a free-electron laser, Physical Review Letters 38 (16) (1977) 892–894.

[18] J. M. J. Madey, Stimulated emission of bremsstrahlung in a periodic magnetic field, Journal of Applied Physics 42 (5) (1971) 1906.

[19] W. Ackermann, G. Asova, V. Ayvazyan, A. Azima, N. Baboi, J. Bähr, V. Balandin, B. Beutner, A. Brandt, A. Bolzmann, R. Brinkmann, O. I. Brovko, M. Castellano, P. Castro, L. Catani, E. Chiadroni, S. Choroba, A. Cianchi, J. T. Costello, D. Cubaynes, J. Dardis, W. Decking, H. Delsim-Hashemi, A. Delserieys, G. Di Pirro, M. Dohlus, S. Düsterer, A. Eckhardt, H. T. Edwards, B. Faatz, J. Feldhaus, K. Flöttmann, J. Frisch, L. Fröhlich, T. Garvey, U. Gensch, C. Gerth, M. Görler, N. Golubeva, H.-J. Grabosch, M. Grecki, O. Grimm, K. Hacker, U. Hahn, J. H. Han, K. Honkavaara, T. Hott, M. Hüning, Y. Ivanisenko, E. Jaeschke, W. Jalmuzna, T. Jezynski, R. Kammering, V. Katalev, K. Kavanagh, E. T. Kennedy, S. Khodyachykh, K. Klose, V. Kocharyan, M. Körfer, M. Kollewe, W. Koprek, S. Korepanov, D. Kostin, M. Krassilnikov, G. Kube, M. Kuhlmann, C. L. S. Lewis, L. Lilje, T. Limberg, D. Lipka, F. Löhl, H. Luna, M. Luong, M. Martins, M. Meyer, P. Michelato, V. Miltchev, W. D. Möller, L. Monaco, W. F. O. Müller, O. Napieralski, O. Napoly, P. Nicolosi, D. Nölle, T. Nuñez, A. Oppelt, C. Pagani, R. Paparella, N. Pchalek, J. Pedregosa-Gutierrez, B. Petersen, B. Petrosyan, G. Petrosyan, L. Petrosyan, J. Pflüger, E. Plönjes, L. Poletto, K. Pozniak, E. Prat, D. Proch, P. Pucyk, P. Radcliffe, H. Redlin, K. Rehlich, M. Richter, M. Roehrs, J. Roensch, R. Romaniuk, M. Ross, J. Rossbach, V. Rybnikov, M. Sachwitz, E. L. Saldin, W. Sandner, H. Schlarb, B. Schmidt, M. Schmitz, P. Schmüser, J. R. Schneider, E. A. Schneidmiller, S. Schnepp, S. Schreiber, M. Seidel, D. Sertore, A. V. Shabunov, C. Simon, S. Simrock, E. Sombrowski, A. A. Sorokin, P. Spanknebel, R. Spesyvtsev, L. Staykov, B. Steffen, F. Stephan, F. Stulle, H. Thom, K. Tiedtke, M. Tischer, S. Toleikis, R. Treusch, D. Trines, I. Tsakov, E. Vogel, T. Weiland, H. Weise, M. Wellhöfer, M. Wendt, I. Will, A. Winter, K. Wittenburg, W. Wurth, P. Yeates, M. V. Yurkov, I. Zagorodnov, K. Zapfe, Operation of a free-electron laser from the extreme ultraviolet to the water window, Nature Photonics 1 (6) (2007) 336–342.

[20] B. Nagler, U. Zastrau, R. R. Fäustlin, S. M. Vinko, T. Whitcher, A. J. Nelson,

R. Sobierajski, J. Krzywinski, J. Chalupsky, E. Abreu, S. Bajt, T. Bornath, T. Burian, H. Chapman, J. Cihelka, T. Döppner, S. Düsterer, T. Dzelzainis, M. Fajardo, E. Förster, C. Fortmann, E. Galtier, S. H. Glenzer, S. Göde, G. Gregori, V. Hajkova, P. Heimann, L. Juha, M. Jurek, F. Y. Khattak, A. R. Khorsand, D. Klinger, M. Kozlova, T. Laarmann, H. J. Lee, R. W. Lee, K.-H. Meiwes-Broer, P. Mercere, W. J. Murphy, A. Przystawik, R. Redmer, H. Reinholz, D. Riley, G. Röpke, F. Rosmej, K. Saksl, R. Schott, R. Thiele, J. Tiggesbäumker, S. Toleikis, T. Tschentscher, I. Uschmann, H. J. Vollmer, J. S. Wark, Turning solid aluminium transparent by intense soft X-ray photoionization, Nature Physics 5 (9) (2009) 693–696.

[21] H. N. Chapman, A. Barty, M. J. Bogan, S. Boutet, M. Frank, S. P. Hau-Riege, S. Marchesini, B. W. Woods, S. Bajt, W. H. Benner, R. A. London, E. Plönjes, M. Kuhlmann, R. Treusch, S. Düsterer, T. Tschentscher, J. R. Schneider, E. Spiller, T. Möller, C. Bostedt, M. Hoener, D. A. Shapiro, K. O. Hodgson, D. van der Spoel, F. Burmeister, M. Bergh, C. Caleman, G. Huldt, M. M. Seibert, F. R. N. C. Maia, R. W. Lee, A. Szöke, N. Timneanu, J. Hajdu, Femtosecond diffractive imaging with a soft-X-ray free-electron laser, Nature Physics 2 (12) (2006) 839–843.

[22] H. N. Chapman, S. P. Hau-Riege, M. J. Bogan, S. Bajt, A. Barty, S. Boutet, S. Marchesini, M. Frank, B. W. Woods, W. H. Benner, R. A. London, U. Rohner, A. Szöke, E. Spiller, T. Möller, C. Bostedt, D. A. Shapiro, M. Kuhlmann, R. Treusch, E. Plönjes, F. Burmeister, M. Bergh, C. Caleman, G. Huldt, M. M. Seibert, J. Hajdu, Femtosecond time-delay X-ray holography, Nature 448 (7154) (2007) 676–679.

[23] P. Emma, R. Akre, J. Arthur, R. Bionta, C. Bostedt, J. Bozek, A. Brachmann, P. Bucksbaum, R. Coffee, F.-J. Decker, Y. Ding, D. Dowell, S. Edstrom, A. Fisher, J. Frisch, S. Gilevich, J. Hastings, G. Hays, P. Hering, Z. Huang, R. Iverson, H. Loos, M. Messerschmidt, A. Miahnahri, S. Moeller, H.-D. Nuhn, G. Pile, D. Ratner, J. Rzepiela, D. Schultz, T. Smith, P. Stefan, H. Tompkins, J. Turner, J. Welch, W. White, J. Wu, G. Yocky, J. Galayda, First lasing and operation of an ångstrom-wavelength free-electron laser, Nature Photonics 4 (9) (2010) 641–647.

[24] E. Allaria, L. Badano, S. Bassanese, F. Capotondi, D. Castronovo, P. Cinquegrana, M. Danailov, G. D'Auria, A. Demidovich, R. De Monte, et al., The fermi free-electron lasers, Journal of synchrotron radiation 22 (3) (2015) 485–491.

[25] T. Ishikawa, H. Aoyagi, T. Asaka, Y. Asano, N. Azumi, T. Bizen, H. Ego, K. Fukami, T. Fukui, Y. Furukawa, et al., A compact x-ray free-electron laser emitting in the sub-angstrom region, Nature Photonics 6 (8) (2012) 540–544.

[26] E. A. Schneidmiller, M. V. Yurkov, in: Photon beam properties at the European XFEL, XFEL.EU TN-2011-006, Hamburg, 2011.

[27] R. Ganter, Swissfel-conceptual design report, Tech. rep., Paul Scherrer Institute (PSI) (2010).

[28] C. Bostedt, S. Boutet, D. M. Fritz, Z. Huang, H. J. Lee, H. T. Lemke, A. Robert, W. F. Schlotter, J. J. Turner, G. J. Williams, Linac coherent light source: the first five years, Reviews of Modern Physics 88 (1) (2016) 015007.

[29] A. M. Lindenberg, J. Larsson, K. Sokolowski-Tinten, K. J. Gaffney, C. Blome,

O. Synnergren, J. Sheppard, C. Caleman, A. G. MacPhee, D. Weinstein, D. P. Lowney, T. K. Allison, T. Matthews, R. W. Falcone, A. L. Cavalieri, D. M. Fritz, S. H. Lee, P. H. Bucksbaum, D. A. Reis, J. Rudati, P. H. Fuoss, C. C. Kao, D. P. Siddons, R. Pahl, J. Als-Nielsen, S. Duesterer, R. Ischebeck, H. Schlarb, H. Schulte-Schrepping, T. Tschentscher, J. Schneider, D. von der Linde, O. Hignette, F. Sette, H. N. Chapman, R. W. Lee, T. N. Hansen, S. Techert, J. S. Wark, M. Bergh, G. Huldt, D. van der Spoel, N. Timneanu, J. Hajdu, R. A. Akre, E. Bong, P. Krejcik, J. Arthur, S. Brennan, K. Luening, J. B. Hastings, Atomic-scale visualization of inertial dynamics, Science 308 (5720) (2005) 392.

[30] K. J. Gaffney, A. M. Lindenberg, J. Larsson, K. Sokolowski-Tinten, C. Blome, O. Synnergren, J. Sheppard, C. Caleman, A. G. MacPhee, D. Weinstein, D. P. Lowney, T. Allison, T. Matthews, R. W. Falcone, A. L. Cavalieri, D. M. Fritz, S. H. Lee, P. H. Bucksbaum, D. A. Reis, J. Rudati, A. T. Macrander, P. H. Fuoss, C. C. Kao, D. P. Siddons, R. Pahl, K. Moffat, J. Als-Nielsen, S. Duesterer, R. Ischebeck, H. Schlarb, H. Schulte-Schrepping, J. Schneider, D. von der Linde, O. Hignette, F. Sette, H. N. Chapman, R. W. Lee, T. N. Hansen, J. S. Wark, M. Bergh, G. Huldt, D. van der Spoel, N. Timneanu, J. Hajdu, R. A. Akre, E. Bong, P. Krejcik, J. Arthur, S. Brennan, K. Luening, J. B. Hastings, Observation of structural anisotropy and the onset of liquidlike motion during the nonthermal melting of InSb, Physical Review Letters 95 (12) (2005) 125701.

[31] S. M. Vinko, U. Zastrau, S. Mazevet, J. Andreasson, S. Bajt, T. Burian, J. Chalupsky, H. N. Chapman, J. Cihelka, D. Doria, T. Döppner, S. Düsterer, T. Dzelzainis, R. R. Fäustlin, C. Fortmann, E. Förster, E. Galtier, S. H. Glenzer, S. Göde, G. Gregori, J. Hajdu, V. Hajkova, P. A. Heimann, R. Irsig, L. Juha, M. Jurek, J. Krzywinski, T. Laarmann, H. J. Lee, R. W. Lee, B. Li, K.-H. Meiwes-Broer, J. P. Mithen, B. Nagler, A. J. Nelson, A. Przystawik, R. Redmer, D. Riley, F. Rosmej, R. Sobierajski, F. Tavella, R. Thiele, J. Tiggesbäumker, S. Toleikis, T. Tschentscher, L. Vysin, T. J. Whitcher, S. White, J. S. Wark, Electronic structure of an XUV photogenerated solid-density aluminum plasma, Physical Review Letters 104 (22) (2010) 225001.

[32] L. Young, E. P. Kanter, B. Krässig, Y. Li, A. M. March, S. T. Pratt, R. Santra, S. H. Southworth, N. Rohringer, L. F. DiMauro, G. Doumy, C. A. Roedig, N. Berrah, L. Fang, M. Hoener, P. H. Bucksbaum, J. P. Cryan, S. Ghimire, J. M. Glownia, D. A. Reis, J. D. Bozek, C. Bostedt, M. Messerschmidt, Femtosecond electronic response of atoms to ultra-intense X-rays, Nature 466 (7302) (2010) 56–61.

[33] T. Gorkhover, M. Adolph, D. Rupp, S. Schorb, S. W. Epp, B. Erk, L. Foucar, R. Hartmann, N. Kimmel, K.-U. Kühnel, D. Rolles, B. Rudek, A. Rudenko, R. Andritschke, A. Aquila, J. D. Bozek, N. Coppola, T. Erke, F. Filsinger, H. Gorke, H. Graafsma, L. Gumprecht, G. Hauser, S. Herrmann, H. Hirsemann, A. Hömke, P. Holl, C. Kaiser, F. Krasniqi, J.-H. Meyer, M. Matysek, M. Messerschmidt, D. Miessner, B. Nilsson, D. Pietschner, G. Potdevin, C. Reich, G. Schaller, C. Schmidt, F. Schopper, C. D. Schröter, J. Schulz, H. Soltau, G. Weidenspointner, I. Schlichting, L. Strüder, J. Ullrich, T. Möller, C. Bostedt, Nanoplasma dynamics of single large xenon clusters irradiated with superintense X-ray pulses from the linac coherent light source free-electron

laser, Physical Review Letters 108 (24) (2012) 245005.
[34] I. Schlichting, Serial femtosecond crystallography: the first five years, IUCrJ 2 (2) (2015) 246–255.
[35] L. Redecke, K. Nass, D. P. DePonte, T. A. White, D. Rehders, A. Barty, F. Stellato, M. Liang, T. R. M. Barends, S. Boutet, G. J. Williams, M. Messerschmidt, M. M. Seibert, A. Aquila, D. Arnlund, S. Bajt, T. Barth, M. J. Bogan, C. Caleman, T.-C. Chao, R. B. Doak, H. Fleckenstein, M. Frank, R. Fromme, L. Galli, I. Grotjohann, M. S. Hunter, L. C. Johansson, S. Kassemeyer, G. Katona, R. A. Kirian, R. Koopmann, C. Kupitz, L. Lomb, A. V. Martin, S. Mogk, R. Neutze, R. L. Shoeman, J. Steinbrener, N. Timneanu, D. Wang, U. Weierstall, N. A. Zatsepin, J. C. H. Spence, P. Fromme, I. Schlichting, M. Duszenko, C. Betzel, H. N. Chapman, Natively inhibited Trypanosoma brucei cathepsin B structure determined by using an X-ray laser, Science 339 (6116) (2012) 227–230.
[36] A. Aquila, M. S. Hunter, R. B. Doak, R. A. Kirian, P. Fromme, T. A. White, J. Andreasson, D. Arnlund, S. Bajt, T. R. M. Barends, M. Barthelmess, M. J. Bogan, C. Bostedt, H. Bottin, J. D. Bozek, C. Caleman, N. Coppola, J. Davidsson, D. P. DePonte, V. Elser, S. W. Epp, B. Erk, H. Fleckenstein, L. Foucar, M. Frank, R. Fromme, H. Graafsma, I. Grotjohann, L. Gumprecht, J. Hajdu, C. Y. Hampton, A. Hartmann, R. Hartmann, S. Hau-Riege, G. Hauser, H. Hirsemann, P. Holl, J. M. Holton, A. Hömke, L. Johansson, N. Kimmel, S. Kassemeyer, F. Krasniqi, K.-U. Kühnel, M. Liang, L. Lomb, E. Malmerberg, S. Marchesini, A. V. Martin, F. R. Maia, M. Messerschmidt, K. Nass, C. Reich, R. Neutze, D. Rolles, B. Rudek, A. Rudenko, I. Schlichting, C. Schmidt, K. E. Schmidt, J. Schulz, M. M. Seibert, R. L. Shoeman, R. Sierra, H. Soltau, D. Starodub, F. Stellato, S. Stern, L. Strüder, N. Timneanu, J. Ullrich, X. Wang, G. J. Williams, G. Weidenspointner, U. Weierstall, C. Wunderer, A. Barty, J. C. H. Spence, H. N. Chapman, Time-resolved protein nanocrystallography using an X-ray free-electron laser, Optics Express 20 (3) (2012) 2706.
[37] H. N. Chapman, C. Caleman, N. Timneanu, Diffraction before destruction, Philosophical Transactions of the Royal Society B: Biological Sciences 369 (1647) (2014) 20130313–20130313.
[38] C. Caleman, G. Huldt, F. R. N. C. Maia, C. Ortiz, F. G. Parak, J. Hajdu, D. van der Spoel, H. N. Chapman, N. Timneanu, On the feasibility of nanocrystal imaging using intense and ultrashort X-ray pulses, ACS Nano 5 (1) (2011) 139–146.
[39] S. P. Hau-Riege, High-intensity X-rays–interaction with matter: processes in plasmas, clusters, molecules, and solids, Wiley-VCH, Weinheim, 2011.
[40] A. Einstein, Über einen die Erzeugung und Verwandlung des Lichtes betreffenden heuristischen Gesichtspunkt, Annalen der Physik 322 (6) (1905) 132–148.
[41] R. A. Millikan, A Direct Determination of " h .", Physical Review 4 (1) (1914) 73–75.
[42] L. Meitner, Über die Entstehung der β-Strahl-Spektren radioaktiver Substanzen, Zeitschrift für Physik 9 (1) (1922) 131–144.
[43] P. Auger, Sur les rayons β secondaires produits dans un gaz par des rayons X, C.R.A.S. 117 (1923) 169–171.

[44] A. Classen, K. Ayyer, H. N. Chapman, R. Röhlsberger, J. von Zanthier, Incoherent diffractive imaging via intensity correlations of hard X-rays, Physical Review Letters 119 (5) (2017) 053401.
[45] M. Bergh, Interaction of Ultrashort X-ray Pulses with Material, Ph.D. thesis, Acta Universitatis Upsaliensis Acta Universitatis Upsaliensis, Uppsala, oCLC: 225809654 (2007).
[46] M. Gabrysch, E. Marklund, J. Hajdu, D. J. Twitchen, J. Rudati, A. M. Lindenberg, C. Caleman, R. W. Falcone, T. Tschentscher, K. Moffat, P. H. Bucksbaum, J. Als-Nielsen, A. J. Nelson, D. P. Siddons, P. J. Emma, P. Krejcik, H. Schlarb, J. Arthur, S. Brennan, J. Hastings, J. Isberg, Formation of secondary electron cascades in single-crystalline plasma-deposited diamond upon exposure to femtosecond x-ray pulses, Journal of Applied Physics 103 (6) (2008) 064909.
[47] S. P. Hau-Riege, Nonequilibrium electron dynamics in materials driven by high-intensity x-ray pulses, Physical Review E 87 (5) (2013) 053102.
[48] S. Hau-Riege, R. London, A. Szoke, Dynamics of biological molecules irradiated by short x-ray pulses, Physical Review E 69 (5) (2004) 051906.
[49] M. Bergh, N. Tîmneanu, D. van der Spoel, Model for the dynamics of a water cluster in an x-ray free electron laser beam, Physical Review E 70 (5) (2004) 051904.
[50] H. G. Moseley, XCIII. The high-frequency spectra of the elements, The London, Edinburgh, and Dublin Philosophical Magazine and Journal of Science 26 (156) (1913) 1024–1034.
[51] R. Piron, F. Gilleron, Y. Aglitskiy, H.-K. Chung, C. Fontes, S. Hansen, O. Marchuk, H. Scott, E. Stambulchik, Y. Ralchenko, Review of the 9th NLTE code comparison workshop, High Energy Density Physics 23 (2017) 38–47.
[52] H. A. Scott, R. W. Mayle, GLF - A simulation code for X-ray lasers, Applied Physics B Laser and Optics 58 (1) (1994) 35–43.
[53] H. A. Scott, Cretin—a radiative transfer capability for laboratory plasmas, Journal of Quantitative Spectroscopy and Radiative Transfer 71 (2-6) (2001) 689–701.
[54] J. C. Stewart, K. D. Pyatt, Lowering of ionization potentials in plasmas, Astrophys. J. 144 (1966) 1203.
[55] F. R. Graziani, V. S. Batista, L. X. Benedict, J. I. Castor, H. Chen, S. N. Chen, C. A. Fichtl, J. N. Glosli, P. E. Grabowski, A. T. Graf, S. P. Hau-Riege, A. U. Hazi, S. A. Khairallah, L. Krauss, A. B. Langdon, R. A. London, A. Markmann, M. S. Murillo, D. F. Richards, H. A. Scott, R. Shepherd, L. G. Stanton, F. H. Streitz, M. P. Surh, J. C. Weisheit, H. D. Whitley, Large-scale molecular dynamics simulations of dense plasmas: The Cimarron Project, High Energy Density Physics 8 (1) (2012) 105–131.
[56] B. F. Murphy, T. Osipov, Z. Jurek, L. Fang, S.-K. Son, M. Mucke, J. Eland, V. Zhaunerchyk, R. Feifel, L. Avaldi, P. Bolognesi, C. Bostedt, J. D. Bozek, J. Grilj, M. Guehr, L. J. Frasinski, J. Glownia, D. T. Ha, K. Hoffmann, E. Kukk, B. K. McFarland, C. Miron, E. Sistrunk, R. J. Squibb, K. Ueda, R. Santra, N. Berrah, Femtosecond X-ray-induced explosion of C60 at extreme intensity, Nature Communications 5 (2014) 4281.
[57] Z. Jurek, S.-K. Son, B. Ziaja, R. Santra, *XMDYN* and *XATOM* : versatile

simulation tools for quantitative modeling of X-ray free-electron laser induced dynamics of matter, Journal of Applied Crystallography 49 (3) (2016) 1048–1056.
[58] C. Caleman, M. Bergh, H. A. Scott, J. C. Spence, H. N. Chapman, N. Tîmneanu, Simulations of radiation damage in biomolecular nanocrystals induced by femtosecond X-ray pulses, Journal of Modern Optics 58 (16) (2011) 1486–1497.
[59] S.-K. Son, H. N. Chapman, R. Santra, Multiwavelength Anomalous Diffraction at High X-Ray Intensity, Physical Review Letters 107 (21) (2011) 218102.
[60] C. Caleman, N. Tîmneanu, A. V. Martin, T. A. White, H. A. Scott, A. Barty, A. Aquila, H. N. Chapman, Modeling of XFEL induced ionization and atomic displacement in protein nanocrystals, in: Proc. SPIE, Vol. 8504, 2012, p. 85040H.
[61] S. Hau-Riege, X-ray atomic scattering factors of low-Z ions with a core hole, Physical Review A 76 (4) (2007) 042511.
[62] D. T. Cromer, J. B. Mann, X-ray scattering factors computed from numerical Hartree–Fock wave functions, Acta Crystallographica Section A 24 (2) (1968) 321–324.
[63] D. L. Book, NRL (Naval Research Laboratory) plasma formulary, revised (2007).
[64] E. Lindahl, B. A. Hess, D. van der Spoel, GROMACS 3.0: A package for molecular simulation and trajectory analysis, J. Mol. Mod. 7 (2001) 306–317.
[65] C. Caleman, G. Huldt, C. Ortiz, F. R. N. C. Maia, F. G. Parak, J. Hajdu, D. van der Spoel, H. N. Chapman, N. Tîmneanu, On the feasibility of nanocrystal imaging using intense and ultrashort x-ray pulses, ACS Nano 5 (2011) 139–146.
[66] H. J. C. Berendsen, J. R. Grigera, T. P. Straatsma, The missing term in effective pair potentials, The Journal of Physical Chemistry 91 (24) (1987) 6269–6271.
[67] A. D. MacKerell, D. Bashford, M. Bellott, R. L. Dunbrack, J. D. Evanseck, M. J. Field, S. Fischer, J. Gao, H. Guo, S. Ha, D. Joseph-McCarthy, L. Kuchnir, K. Kuczera, F. T. K. Lau, C. Mattos, S. Michnick, T. Ngo, D. T. Nguyen, B. Prodhom, W. E. Reiher, B. Roux, M. Schlenkrich, J. C. Smith, R. Stote, J. Straub, M. Watanabe, J. Wiórkiewicz-Kuczera, D. Yin, M. Karplus, All-Atom Empirical Potential for Molecular Modeling and Dynamics Studies of Proteins, The Journal of Physical Chemistry B 102 (18) (1998) 3586–3616.
[68] P. M. Morse, Diatomic molecules according to the wave mechanics. II. vibrational levels., Phys. Rev. 34 (1929) 57–64.
[69] S. Boutet, G. J Williams, The Coherent X-ray Imaging (CXI) instrument at the Linac Coherent Light Source (LCLS), New Journal of Physics 12 (3) (2010) 035024.
[70] D. P. DePonte, U. Weierstall, K. Schmidt, J. Warner, D. Starodub, J. C. H. Spence, R. B. Doak, Gas dynamic virtual nozzle for generation of microscopic droplet streams, Journal of Physics D: Applied Physics 41 (19) (2008) 195505.
[71] U. Weierstall, J. C. H. Spence, R. B. Doak, Injector for scattering measurements on fully solvated biospecies, Review of Scientific Instruments 83 (3) (2012) 035108.
[72] S. Moeller, J. Arthur, A. Brachmann, R. Coffee, F.-J. Decker, Y. Ding,

D. Dowell, S. Edstrom, P. Emma, Y. Feng, A. Fisher, J. Frisch, J. Galayda, S. Gilevich, J. Hastings, G. Hays, P. Hering, Z. Huang, R. Iverson, J. Krzywinski, S. Lewis, H. Loos, M. Messerschmidt, A. Miahnahri, H.-D. Nuhn, D. Ratner, J. Rzepiela, D. Schultz, T. Smith, P. Stefan, H. Tompkins, J. Turner, J. Welch, B. White, J. Wu, G. Yocky, R. Bionta, E. Ables, B. Abraham, C. Gardener, K. Fong, S. Friedrich, S. Hau-Riege, K. Kishiyama, T. McCarville, D. McMahon, M. McKernan, L. Ott, M. Pivovaroff, J. Robinson, D. Ryutov, S. Shen, R. Soufli, G. Pile, Photon beamlines and diagnostics at LCLS, Nuclear Instruments and Methods in Physics Research Section A: Accelerators, Spectrometers, Detectors and Associated Equipment 635 (1) (2011) S6–S11.

[73] T. B. van Driel, S. Herrmann, G. Carini, M. M. Nielsen, H. T. Lemke, Correction of complex nonlinear signal response from a pixel array detector, Journal of Synchrotron Radiation 22 (3) (2015) 584–591.

[74] C. A. Stan, D. Milathianaki, H. Laksmono, R. G. Sierra, T. A. McQueen, M. Messerschmidt, G. J. Williams, J. E. Koglin, T. J. Lane, M. J. Hayes, S. A. H. Guillet, M. Liang, A. L. Aquila, P. R. Willmott, J. S. Robinson, K. L. Gumerlock, S. Botha, K. Nass, I. Schlichting, R. L. Shoeman, H. A. Stone, S. Boutet, Liquid explosions induced by X-ray laser pulses, Nature Physics 12 (10) (2016) 966–971.

[75] Z. Dauter, K. S. Wilson, L. C. Sieker, J. Meyer, J.-M. Moulis, Atomic resolution (0.94 å) structure of *Clostridium acidurici* ferredoxin. detailed geometry of [4fe-4s] clusters in a protein, Biochemistry 36 (51) (1997) 16065–16073.

[76] R. Neutze, R. Wouts, D. van der Spoel, E. Weckert, J. Hajdu, Potential for biomolecular imaging with femtosecond X-ray pulses, Nature 406 (6797) (2000) 752–757.

[77] I. Waller, Zur frage der einwirkung der wärmebewegung auf die interferenz von röntgenstrahlen, Zeitschrift für Physik A Hadrons and Nuclei 17 (1) (1923) 398–408.

[78] K. Tiedtke, A. Azima, N. von Bargen, L. Bittner, S. Bonfigt, S. Düsterer, B. Faatz, U. Frühling, M. Gensch, C. Gerth, N. Guerassimova, U. Hahn, T. Hans, M. Hesse, K. Honkavaar, U. Jastrow, P. Juranic, S. Kapitzki, B. Keitel, T. Kracht, M. Kuhlmann, W. B. Li, M. Martins, T. Núñez, E. Plönjes, H. Redlin, E. L. Saldin, E. A. Schneidmiller, J. R. Schneider, S. Schreiber, N. Stojanovic, F. Tavella, S. Toleikis, R. Treusch, H. Weigelt, M. Wellhöfer, H. Wabnitz, M. V. Yurkov, J. Feldhaus, The soft x-ray free-electron laser FLASH at DESY: beamlines, diagnostics and end-stations, New Journal of Physics 11 (2) (2009) 023029.

[79] S. Düsterer, P. Radcliffe, C. Bostedt, J. Bozek, A. L. Cavalieri, R. Coffee, J. T. Costello, D. Cubaynes, L. F. DiMauro, Y. Ding, G. Doumy, F. Grüner, W. Helml, W. Schweinberger, R. Kienberger, A. R. Maier, M. Messerschmidt, V. Richardson, C. Roedig, T. Tschentscher, M. Meyer, Femtosecond x-ray pulse length characterization at the Linac Coherent Light Source free-electron laser, New Journal of Physics 13 (9) (2011) 093024.

[80] C. Behrens, F.-J. Decker, Y. Ding, V. A. Dolgashev, J. Frisch, Z. Huang, P. Krejcik, H. Loos, A. Lutman, T. J. Maxwell, J. Turner, J. Wang, M.-H. Wang, J. Welch, J. Wu, Few-femtosecond time-resolved measurements of X-ray

free-electron lasers, Nature Communications 5 (2014) 3762.
[81] E.A. Schneidmiller, M.V. Yurkov, Photon beam properties at the European XFEL, Tech. rep., Deutsches Elektronen-Synchrotron, DESY, Hamburg (2011).
[82] Z. T. Zhao, D. Wang, J. H. Chen, Z. H. Chen, H. X. Deng, J. G. Ding, C. Feng, Q. Gu, M. M. Huang, T. H. Lan, Y. B. Leng, D. G. Li, G. Q. Lin, B. Liu, E. Prat, X. T. Wang, Z. S. Wang, K. R. Ye, L. Y. Yu, H. O. Zhang, J. Q. Zhang, M. Zhang, M. Zhang, T. Zhang, S. P. Zhong, Q. G. Zhou, First lasing of an echo-enabled harmonic generation free-electron laser, Nature Photonics 6 (6) (2012) 360–363.
[83] E. Allaria, R. Appio, L. Badano, W. Barletta, S. Bassanese, S. Biedron, A. Borga, E. Busetto, D. Castronovo, P. Cinquegrana, S. Cleva, D. Cocco, M. Cornacchia, P. Craievich, I. Cudin, G. D'Auria, M. Dal Forno, M. Danailov, R. De Monte, G. De Ninno, P. Delgiusto, A. Demidovich, S. Di Mitri, B. Diviacco, A. Fabris, R. Fabris, W. Fawley, M. Ferianis, E. Ferrari, S. Ferry, L. Froehlich, P. Furlan, G. Gaio, F. Gelmetti, L. Giannessi, M. Giannini, R. Gobessi, R. Ivanov, E. Karantzoulis, M. Lonza, A. Lutman, B. Mahieu, M. Milloch, S. Milton, M. Musardo, I. Nikolov, S. Noe, F. Parmigiani, G. Penco, M. Petronio, L. Pivetta, M. Predonzani, F. Rossi, L. Rumiz, A. Salom, C. Scafuri, C. Serpico, P. Sigalotti, S. Spampinati, C. Spezzani, M. Svandrlik, C. Svetina, S. Tazzari, M. Trovo, R. Umer, A. Vascotto, M. Veronese, R. Visintini, M. Zaccaria, D. Zangrando, M. Zangrando, Highly coherent and stable pulses from the FERMI seeded free-electron laser in the extreme ultraviolet, Nature Photonics 6 (10) (2012) 699–704.
[84] W. Helml, A. R. Maier, W. Schweinberger, I. Grguraš, P. Radcliffe, G. Doumy, C. Roedig, J. Gagnon, M. Messerschmidt, S. Schorb, C. Bostedt, F. Grüner, L. F. DiMauro, D. Cubaynes, J. D. Bozek, T. Tschentscher, J. T. Costello, M. Meyer, R. Coffee, S. Düsterer, A. L. Cavalieri, R. Kienberger, Measuring the temporal structure of few-femtosecond free-electron laser X-ray pulses directly in the time domain, Nature Photonics 8 (12) (2014) 950–957.
[85] B. Henke, E. Gullikson, J. Davis, X-Ray Interactions: Photoabsorption, Scattering, Transmission, and Reflection at E = 50-30,000 eV, Z = 1-92, Atomic Data and Nuclear Data Tables 54 (2) (1993) 181–342.
[86] F. R. Maia, J. Hajdu, The trickle before the torrent—diffraction data from X-ray lasers, Scientific Data 3 (2016) 160059.
[87] J. C. H. Spence, XFELs for structure and dynamics in biology, IUCrJ 4 (4) (2017) 322–339.
[88] The runners-up, Science 338 (6114) (2012) 1525–1532.

This doctoral thesis is in part based upon the licentiate thesis "Femtosecond Dynamics in Water and Biological Materials with an X-Ray Laser" by the same author presented in 2016 at Uppsala University.

Acta Universitatis Upsaliensis

Digital Comprehensive Summaries of Uppsala Dissertations from the Faculty of Science and Technology 1592

Editor: The Dean of the Faculty of Science and Technology

A doctoral dissertation from the Faculty of Science and Technology, Uppsala University, is usually a summary of a number of papers. A few copies of the complete dissertation are kept at major Swedish research libraries, while the summary alone is distributed internationally through the series Digital Comprehensive Summaries of Uppsala Dissertations from the Faculty of Science and Technology. (Prior to January, 2005, the series was published under the title "Comprehensive Summaries of Uppsala Dissertations from the Faculty of Science and Technology".)

Distribution: publications.uu.se
urn:nbn:se:uu:diva-331936

ACTA
UNIVERSITATIS
UPSALIENSIS
UPPSALA
2017